Fault rupture propagation through stratified sand-clay deposits and engineered earth structures: a meshfree and critical-state modeling approach

Enrique M. del Castillo¹, Alomir H. Fávero Neto², and Ronaldo I. Borja^{1*}.

Summary. Permanent deformation and uplift caused by fault rupture is one of the most significant hazards posed by earthquakes on the built environment. In this paper, we use Smoothed Particle Hydrodynamics (SPH) to explore the effects of soil layering or stratification on the trajectories and deformation patterns caused by rupturing reverse faults in bedrock, as well as in the foundations of engineered earth structures. SPH is a continuum meshfree numerical method highly adept at modeling large deformation problems in geotechnics. Through the use of constitutive models involving softening behavior as well as critical state type models, we isolate the effects of rigid body rotation from critical state behavior of soil in helping explain the frequently observed rotation of shear bands emanating from the bedrock fault. This analysis is facilitated by the fact that the SPH method allows us to track the propagation of shear bands over substantial amounts of vertical uplift (more than 50% of the total height of the soil deposit), far beyond many previous computational studies employing the finite element method (FEM). We observe and characterize various emergent features including fault bifurcations, stunted faults, and tension cracking, while providing insights on practical guidelines regarding the potential surface distortion width, and the critical amount of fault displacement required for surface rupture depending on the multilayered constitution of the soil deposit. Finally, we predict the expected amount of surface distortion and internal damage to earthen embankments depending on varying fault location and soil makeup.

Keywords. Reverse fault rupture, Stratified soils, Critical state plasticity, Meshfree continuum methods, Smoothed particle hydrodynamics

1 Introduction

Since the landmark Kocaeli, Düzce (Turkey), and Chi-Chi (Taiwan) earthquakes of 1999, a large number of earthquakes including most recently the 2016 Kumamoto, Japan earthquake [73], the 2018 Palu, Indonesia earthquake [82], and the 2023 Turkey-Syria earthquake [41], have demonstrated the destructive potential of fault surface rupture on infrastructure and the built environment. In the Chi-Chi earthquake alone, more than 30% of all damage suffered by buildings was caused by the propagation of faults in bedrock through the overlying soil deposits, and the ensuing surface rupture, uplift, and scarp formation [86]. Earth structures, such as road embankments, embankment dams, or levees, while less brittle than their concrete counterparts, are also vulnerable to fault rupture occurring in their foundations as the rupture can continue across the earthen material in the form of shear zones or slip planes, leading to significant damage or even full failure of the embankment abutments [42], [59].

In this study, the effects of soil stratification on the propagation properties (orientation and faulting patterns) of shallow-lying reverse faults in bedrock and in the foundations of earthen embankments, as well as the resulting soil and embankment deformation, are considered by performing numerical simulations using smoothed particle hydrodynamics (SPH), a meshfree Lagrangian method, well-suited for handling large deformations and the post-failure behavior of geomaterials [21, 32, 58]. The meshfree nature coupled

¹Department of Civil and Environmental Engineering, Stanford University, Stanford, CA 94305, USA,

²Department of Civil and Environmental Engineering, Bucknell University, Lewisburg, PA 17837, USA,

^{*}Corresponding author, e-mail: borja@stanford.edu

with SPH's ability to capture strain localization without any extra enhancements, makes the method ideal for modeling fault propagation past the initial point of surface rupture [23, 52, 84]. In the past, most computational studies using the finite element method (FEM) have only simulated vertical uplift up to around 4 to 10% of the total thickness of the soil deposit [12, 43], whereas in this study, the SPH method has no restriction on the amount of slip sustained on the fault. Furthermore, when modeling discontinuities associated with faulting and strain localization, mesh based methods such as FEM either require the fault path to be predetermined [47, 67, 68] or necessitate enhancements such as those seen in the phase field [1, 29, 39, 40, 75], extended finite elements [37, 55, 80], strong discontinuity [9, 64, 74], or gradient damage [11, 16, 27, 56] methods. As with these mentioned improvements over basic FEM, the SPH method has the advantage that it possesses non-local properties which help alleviate the pathological mesh sensitivity associated with strain softening and localization. Additionally, SPH is more computationally efficient than non-continuum particle methods such as the discrete element method (DEM) [45, 63, 83], another method that has been used for modeling fracture, faulting, and strain localization in granular geomaterials [21, 26, 30].

The focus of this paper is on comparing fault rupture in loose sands, cohesive soft sedimentary rock, the seldom studied soft clays, as well as layered soil deposits consisting of combinations of these types of geomaterials. The soft clays are modeled using the Modified Cam Clay (MCC) constitutive model to capture the influence of the degree of soil compaction on the fault rupture process. In doing so we use a variation of the MCC closest point projection return mapping algorithm amenable to the SPH method developed in the authors' previous work [25].

In Section 2, we provide a literature review on studies of fault propagation and surface rupture, as well as an overview of the different techniques previously used to study this problem. In Section 3.1, we introduce the initial boundary value problem we are solving, as well as the SPH method. An elastoplastic model employing the Drucker-Prager (DP) yield criterion as well as a demonstration of the method's non-local properties under softening are presented in Section 3.2, while the MCC model is summarized in Section 3.3. In Section 4, the results of our SPH simulations of reverse fault propagation through stratified sand-clay and sand-soft rock layered deposits are shown. In Section 5 we model reverse fault rupture underneath the foundations of an earthen embankment to discern the properties controlling the varying deformation patterns and damage sustained. Lastly, these results are discussed in Section 6 and some concluding thoughts and future work are provided in Section 7.

2 Previous Work

The primary concerns for the engineer or geoscientist when considering the implications of the propagation of a fault in bedrock include: (a) determining the number and location of surface ruptures, (b) the orientation and trajectory of the ruptures, (c) the extent of surface elevation change, (d) the critical amount of fault slip or vertical displacement required for initial surface rupture, and (e) the width of the affected post-rupture surface distortion zone. Previous works have explored the effects of soil properties such as soil strength, dilatancy, and stiffness [6, 23, 50, 77], interactions between fault ruptures and foundations [5, 48], underground infrastructure [7, 15, 44, 89], or topography on the previously mentioned quantities [71]. Yet very few studies have gone beyond single-layered homogeneous soil deposits, which are not representative of the heterogeneous, multilayered stratified soil deposits overlying bedrock found in nature.

The work by Tali and coauthors [77] employed centrifuge experiments to model the rupture of faults through double-layered setups with alternating sand or clayey-sand units, to analyze the effects of soil type on the width of the post-rupture surface distortion zone, as well as on the critical vertical fault offset required for initial surface rupture. The centrifuge experiments performed by Hung et al. [38] carried out similar analyses, but instead, looked at loose sand overlying soft rock and varied the ratio of sand to soft rock for each experiment. Garcia and Bray [31] utilized DEM to computationally study the effects of soil stratification with varying densities on the fault rupture geometry. The authors concluded that the width and number of layers played an important role, but that deformation in the stratified models would

ultimately be bounded by the extreme behavior of homogeneous models comprised by the same granular material as one of the individual layers in the multi-layer model. These results were supported by similar findings using the commercial finite difference software FLAC2D [19]. The FEM simulations conducted by Shi and coauthors [70] were used to study the refraction of the fault rupture across intercalated layers of different stiffness, as well as the rate of fault propagation using a non-local model, emphasizing the importance of obtaining discretization independent solutions in the fault propagation process.

Empirical failure surfaces in the shape of logarithmic spirals with the surface rupture orientation given by $45^{\circ} - \psi/2$ with respect to the maximum principal incremental strain direction (Roscoe angle [65]), where ψ is the dilatancy angle of the material, were first proposed by Cole and Lade [18] to capture the trajectory of propagating faults at the point of initial surface rupture for homogeneous soil deposits. However, more recent work has shown that the accuracy of such failure surfaces decreases with increasing slip on the bedrock fault, especially past that required for initial surface rupture [23, 43]. The work of Yao et al. [87, [88]] suggests that hyperbolic spirals with the surface rupture oriented at $45^{\circ} - \phi/2$ (Coulomb angle [20]), where ϕ is the internal friction angle, describe the propagation geometry more accurately, due to the degradation of the dilatancy angle from a peak to a residual or critical state value as a result of softening behavior in the sand. Following similar arguments proposed by Stone and Wood [76], Yao et al. concluded that the initial rupture followed a trajectory similar to that predicted by the logarithmic spiral with the tip orientation controlled by the dilatancy angle, until the dilatancy angle decreases to the critical state value along the rupture path, causing the orientation to be subsequently determined by the friction angle.

All these prior studies used offsets in colored material marker layers to determine the location of the propagating fault tip and the overall fault rupture geometry rather than calculated strain or strain rate fields, and presumably measured the orientations of the faults with respect to the horizontal, not the direction of the maximum principal stress σ_1 (from which the Coulomb angle is measured) or the maximum principal incremental strain direction (from which the Roscoe angle is referenced). The first point is problematic for two reasons: first at small amounts of slip in the bedrock fault, offset in the marker layers is often difficult to discern. Second, faults modeled with sands or other low-cohesion granular materials in analogue or computational scaled models are actually shear bands, which may form without significant visible lateral offset. When extracting continuum deformation fields from a discrete element granular assembly (see 35), the initial fault rupture has been shown to most closely take an orientation given by the Roscoe angle. The SPH simulations presented by the work of Mullet et al. [54], showed that while the initial direction of shear bands in caldera collapses (modeled using the trapdoor problem) was closest to the Roscoe angle, the subsequent evolution of the orientation could only be captured when modeling a transition of the friction and dilatancy angles from a peak to residual value as a function of plastic strain. Because of the continuum nature of the SPH method, the strain fields were easily obtained to be able to track the evolution of shear bands in the caldera collapse simulations.

To determine whether softening behavior was responsible for the poor initial rupture predictions provided by the Roscoe orientation, and given that in our previous work, performed using perfect plasticity, shear bands rotated over progressive fault slip from Roscoe to Arthur $(45^{\circ} - (\psi + \phi)/4)$ to Coulomb angles [23], in [24], we conducted a series of simulations using SPH comparing the results of models of fault rupture in homogeneous soil units employing strain softening versus those with perfect plasticity. In all models, a rotation of fault orientation, measured at the upmost fault/band tip, was observed to change from Roscoe to Arthur to Coulomb inclinations, suggesting that at least in part, the rotation of the fault was a product of rigid body rotation of fully propagated faults due to the boundary conditions, and not only of softening behavior.

To date, the vast majority of studies have modeled fault rupture through sands or loose cohesionless granular materials, and have ignored the presence of cohesive soils, such as clays, which are common soil types overlying bedrock. The work of Bray and coauthors [12] compared results from analogue sandbox-type experiments using clay with finite element method (FEM) simulations using a hyperbolic stress-strain model. However, clays are best characterized by critical state type constitutive models, like the Modified Cam Clay (MCC) model, which account for the volumetric behavior and yielding of clays, in addition to critical-state behavior. The doctoral thesis of Lazarte [42] performed FEM simulations using

the MCC model, but observed that the simulations could not reproduce strain localization in normally consolidated or lightly overconsolidated clays. Because of the paucity of studies focusing on fault rupture in overconsolidated clays, and especially clays underlying loose sands, one of the primary concerns of this paper is to address fault geometry and orientation in such soil deposits, using a true critical state model, and a computational technique (SPH) permissive of simulating large slips on the bedrock fault beyond those achievable in FEM simulations.

3 Methods

3.1 Governing Equations and SPH Discretization

The SPH method is used to solve the conservation of mass and momentum equations, which are the governing equations of the mechanical initial boundary value problem over domain Ω and time t:

$$\dot{\rho} + \rho \nabla \cdot \boldsymbol{v} = 0 \quad \forall \boldsymbol{x} \text{ in } \Omega \times t \tag{1}$$

$$\nabla \cdot \boldsymbol{\sigma} + \boldsymbol{b} = \rho \dot{\boldsymbol{v}} \quad \forall \boldsymbol{x} \text{ in } \Omega \times t$$

where $\dot{\boldsymbol{v}}$ is the material time derivative of the velocity field, \boldsymbol{b} is the body force (gravity) vector, $\dot{\rho}$ is the material time derivative of the density field, and $\boldsymbol{\sigma}$ is the Cauchy stress tensor. The stresses are determined via a large-deformation elastoplastic model $\boxed{10}$ that preserves objectivity of the stress rate by way of the Jaumann rate within the rate-constitutive equation.

The smoothed particle hydrodynamics method is a continuum Lagrangian meshless particle method proposed by Lucy [51] and Gingold and Monaghan [33] in astrophysics. In the method, the continuous problem domain is discretized into a series of particles over which the governing equations are solved, and that also serve as Lagrangian points possessing continuum-level properties such as mass, density, stress, and strain. The particles are arbitrarily distributed and their interaction is dictated by the kernel (weighting) function W, which in this paper is the Wendland C2 kernel. The value of the kernel function depends on the distance between the two particles as well as on a characteristic length scale h, known as the smoothing length.

Given a field function f(x,t), its value can be determined for a particular particle using the following convolution integral over the support or integration domain Ω :

$$\langle f(\boldsymbol{x}) \rangle = \int_{\Omega} f(\boldsymbol{x}') W(\boldsymbol{x} - \boldsymbol{x}', h) d\boldsymbol{x}'$$
 (3)

The continuous integral can be approximated as a summation,

$$\langle f(\boldsymbol{x}) \rangle_i = \sum_{j=1}^N f(\boldsymbol{x}_j) W_{ij} V_j,$$
 (4)

and the first derivative of the field function can be similarly approximated,

$$\langle \nabla f(\boldsymbol{x}) \rangle_i = \sum_{j=1}^N f(\boldsymbol{x}_j) \nabla W_{ij} V_j.$$
 (5)

Here $\langle \cdot \rangle$ denotes an approximation, and the subscript j represents the neighboring particles of the particle of interest i, located at $\boldsymbol{x} = \boldsymbol{x}_i$. Additionally, $W_{ij} = W(|\boldsymbol{x}_i - \boldsymbol{x}_j|, h)$ is the kernel function evaluated for particles i and j, and $V_j = m_j/\rho_j$ is the volume of particle j, where m_j and ρ_j are the mass and density of the particle respectively.

Using the so-called SPH operators presented in Eqs. 4 and 5, the conservation of mass Eq. 1 and momentum Eq. 2 are discretized as follows,

$$\langle \dot{\rho} \rangle_i = \sum_{j=1}^N m_j \left(\boldsymbol{v}_j - \boldsymbol{v}_i \right) \cdot \nabla W_{ij},$$
 (6)

$$\langle \dot{\boldsymbol{v}} \rangle_i = \sum_{j=1}^N m_j \left(\frac{\boldsymbol{\sigma}_i + \boldsymbol{\sigma}_j}{\rho_i \rho_j} \right) \cdot \nabla W_{ij} + \boldsymbol{b}_i.$$
 (7)

It is worth noting that in the summation operators above, since kernel functions are often chosen to have a compact support, N refers to the number of neighbors within the kernel support of particle i, which are far fewer than all the particles in the domain, contributing to a reduction in computational cost.

To avoid any undesired oscillations and improve the stability of the SPH simulations, a numerical damping term known as the artificial viscosity is introduced into the balance of linear momentum equation (Eq. 7) [34]. The artificial viscosity is defined as the tensor $\mathbf{\Pi}_{ij} = \Pi_{ij}\mathbf{1}$, with coefficients $0 \le \alpha_{\pi} \le 0.8$ and $\beta_{\pi} = 0$ in this work, and where

$$\Pi_{ij} = \begin{cases}
\frac{\alpha_{\pi} \bar{c}_{ij} \phi_{ij} - \beta_{\pi} \phi_{ij}^{2}}{\bar{\rho}_{ij}} & \text{for } \boldsymbol{v}_{ij} \cdot \boldsymbol{x}_{ij} < 0, \\
0 & \text{for } \boldsymbol{v}_{ij} \cdot \boldsymbol{x}_{ij} \ge 0,
\end{cases}$$
(8)

with

$$\phi_{ij} = \frac{h_{ij} \boldsymbol{v}_{ij} \cdot \boldsymbol{x}_{ij}}{|\boldsymbol{x}_{ij}|^2 + \eta^2},\tag{9}$$

where for particles i and j, $\bar{c}_{ij} = (c_i + c_j)/2$, $\bar{\rho}_{ij} = (\rho_i + \rho_j)/2$, $h_{ij} = (h_i + h_j)/2$, $\boldsymbol{x}_{ij} = \boldsymbol{x}_i - \boldsymbol{x}_j$, $\boldsymbol{v}_{ij} = \boldsymbol{v}_i - \boldsymbol{v}_j$, and $\eta \sim 0.01h$. Additionally, c is the numerical speed of sound for the particles, ρ is the particle density, and h is the smoothing length. The numerical speed of sound for particle i is calculated as

$$c_i = \max\left(\sqrt{\frac{E}{\rho}}, \sqrt{\frac{K}{\rho}}\right)_i. \tag{10}$$

An additional treatment known as the Monaghan artificial stress (\mathbf{R}_{ij}) is also introduced to avoid particle clamping in zones under tensile stress and is given as,

$$\mathbf{R}_{ij} = f_{ij}^n (\mathbf{R}_i + \mathbf{R}_j) \tag{11}$$

where n depends on the choice of smoothing kernel, typically taking values between 2 and 6, while f_{ij} is a repulsive force term and is expressed as,

$$f_{ij} = \frac{W_{ij}}{W(\Delta, h)} \tag{12}$$

where Δ is the initial interparticle distance. Now, the artificial stress tensor of particle i is linked to the stress tensor following the approach of Gray and Monaghan $\boxed{34}$,

$$\hat{R}_i = \epsilon \frac{\langle -\hat{\sigma}_i \rangle}{\rho_i^2}.\tag{13}$$

Here $\langle \cdot \rangle$ refers to the Macaulay brackets, $\hat{\mathbf{R}}_i$ is the diagonal component of the artificial stress tensor \mathbf{R}_i , $\hat{\boldsymbol{\sigma}}_i$ is the diagonal component of the stress tensor $\boldsymbol{\sigma}_i$, and ϵ is a coefficient with a value of $\epsilon = 0.2$ in this work. To obtain \mathbf{R}_i , $\hat{\mathbf{R}}_i$ must be rotated back into the reference coordinate system (see [13] for details).

A further dissipative damping force is also added into the momentum balance, which takes the final form,

$$\langle \dot{\boldsymbol{v}} \rangle_i = \sum_{i=1}^N m_j \left(\frac{\boldsymbol{\sigma}_i + \boldsymbol{\sigma}_j}{\rho_i \rho_j} + \boldsymbol{\Pi}_{ij} + \boldsymbol{R}_{ij} \right) \cdot \nabla W_{ij} + \boldsymbol{b}_i - c_d \boldsymbol{v}_i, \tag{14}$$

where c_d is the damping coefficient given by $c_d = \xi \sqrt{E/(\rho h^2)}$, with E the elastic modulus of the material, and $0 \le \xi \le 0.05$. Note that artificial viscosity and damping are only used simultaneously for initialization simulations, making use of the higher end values of the proposed coefficients. For the fault propagation simulations, only artificial viscosity is used, with lower values of α_{π} , to avoid over-damping the simulation [14].

For Dirichlet-type boundary treatment, for the velocity, we use the so-called dummy boundary conditions. In this approach, three to four layers of SPH boundary particles are placed in lieu of physical solid walls. These particles pertaining to the boundary are either fixed in space or move at a prescribed velocity, with their stresses determined based on stresses from the particles encompassing the domain, following the formulation presented in [85]. The density and the mass of the dummy particles are kept constant throughout the simulation. It is worth noting that we enforce two types of boundary conditions: (1) no-slip, and (2) free-slip. The former is applied to the bottom of the domain to enforce no-slip in the horizontal direction and no penetration in the vertical direction, while the latter is applied to vertical walls to enforce free-slip in the vertical direction and no penetration in the horizontal direction. For details on the implementation of these boundary conditions the reader is referred to [85]. On the fault-soil interface, the boundary condition formulation of Adami et al., [2] is used where the stress of neighboring soil particles is extrapolated onto the boundary particles. Our previous work has shown that under quasistatic loading, this type of boundary condition displays an effective frictional response proportional to the internal friction angle of the soil [22].

The simulation is evolved dynamically and explicitly in time and we use a semi-implicit time integration scheme due to its optimal conservation characteristics [78]. In this scheme, the particle velocity is updated first, followed by its position and density, while the time step, $\Delta t = t_{n+1} - t_n$, must satisfy the Courant–Friedrichs–Lewy (CFL) condition to ensure stability of the simulation:

$$\Delta t = C_0 \frac{h}{c_s},\tag{15}$$

where C_0 is the CFL coefficient, here taken as 0.1, and $c_s = \sqrt{E_0/\rho_0}$ is the numerical sound speed of the material, with E_0 and ρ_0 the reference elastic modulus and mass density of the material, respectively.

In this paper, our parallel SPH code GEOSPH built on the open-source framework PySPH [61] is employed to perform our simulations. For more details regarding the code, its implementation, and past applications, the reader is referred to [22, 23, 25, 27, 28]. For a complete overview of the SPH method, its formulations and derivations, the reader is pointed to [13, 14, 49, 78]. In what follows, we will provide further details on the constitutive models used in our work.

3.2 Drucker-Prager (D-P) model

The Drucker-Prager (D-P) yield criterion is a two invariant smooth approximation of the Mohr-Coulomb (M-C) yield surface that plots as a circle in the deviatoric plane, and can be fitted either to the tension or compression corners of the hexagonal M-C yield surface. Here, a non-associative flow rule is employed, as it has been shown to best describe the behavior of geomaterials. In this study, the D-P criterion is used to model the behavior of loose sands. For details regarding its implementation in the context of the SPH method see [23]. The D-P model following non-associative flow is characterized by three main parameters, the dilatancy angle ψ , and the two M-C parameters, namely the friction angle ϕ , and the cohesion c. The dilatancy angle ψ determines the direction of plastic flow, such that $\psi = \phi$ implies normality of the plastic flow (associative behavior).

To capture the strain softening response of the material, an isotropic softening model is employed where the mobilized friction and dilatancy angles of the material are degraded from a peak (ϕ_{max} and ψ_{max}) to a residual value (ϕ_{res} and $\psi_{\text{res}} = 0$) as a linear function of the octahedral plastic shear strain (γ_{oct}^p) following the method of Anastasopoulos et al. [6]:

$$\phi_{\text{mob}} = \begin{cases} \phi_{\text{max}} - (\phi_{\text{max}} - \phi_{\text{res}}) \frac{\gamma_{\text{oct}}^p}{\gamma_f^p} & \text{for } 0 \le \gamma_{\text{oct}}^p < \gamma_f^p\\ \phi_{\text{res}} & \text{for } \gamma_{\text{oct}}^p \ge \gamma_f^p \end{cases}$$
(16)

$$\psi_{\text{mob}} = \begin{cases} \psi_{\text{max}} \left(1 - \frac{\gamma_{\text{oct}}^p}{\gamma_f^p} \right) & \text{for } 0 \le \gamma_{\text{oct}}^p < \gamma_f^p \\ \psi_{\text{res}} & \text{for } \gamma_{\text{oct}}^p \ge \gamma_f^p \end{cases}$$

$$(17)$$

In the softening model, γ_f^p is the threshold value of the plastic octahedral shear strain at which softening terminates in a direct shear test of the material. Specifically, if δx_y is the amount of horizontal displacement required for initial yielding in the direct shear test, and δx_{max} is the amount of horizontal displacement at which peak shear stress is obtained, then the amount of plastic shear strain at the point of maximum shear stress is $\gamma_{\text{max}}^p = (\delta x_{\text{max}} - \delta x_y)/D$, assuming that localization has not yet occurred, and the shear strain is distributed evenly over the depth D of the shear box. The post-peak softening behavior that ensues in the direct shear test encourages localization of the strain into a narrow tabular shear band of width $d_B = 16d_{50}$, where d_{50} is the mean grain size of the sand [53]. Therefore, the total final plastic strain sustained up to the point of residual strength at the culmination of the softening response is,

$$\gamma_f^p = \gamma_{\text{max}}^p + \frac{\delta x_f - \delta x_{\text{max}}}{d_B} \tag{18}$$

where δx_f is the horizontal displacement at the end of softening. Here the plastic shear strain outside of the shear band has been assumed to be negligible [72].

Boundary value problems involving strain softening often exhibit pathological sensitivity to the level of discretization. In the SPH method, the width of the computationally generated shear band will satisfy $d_{B,\text{SPH}} \geq h = k_h \Delta$, where Δ is the initial interparticle distance and k_h is the smoothing length factor. We can define a non-dimensional parameter,

$$\zeta = \frac{\gamma_B}{\gamma_{\rm SPH}} = \frac{\delta x/d_B}{\delta x/h} = \frac{h}{d_B},\tag{19}$$

where γ_{SPH} is the shear strain across a SPH particle interpolation and γ_B is the shear strain across a shear band. The parameter ζ is introduced to correct the constitutive model whenever $h \neq d_B$. Therefore, the post-peak contributions to the plastic shear strain can be scaled by ζ yielding,

$$\gamma_f^p = \gamma_{\text{max}}^p + \frac{\delta x_f - \delta x_{\text{max}}}{d_B} \cdot \frac{1}{\zeta} = \gamma_{\text{max}}^p + \frac{\delta x_f - \delta x_{\text{max}}}{h}.$$
 (20)

A further upshot of the SPH method is that because of the non-local properties introduced into the method as a consequence of the smoothing length h which is in effect, a numerical characteristic length scale, the sensitivity of the width of the shear band to the spatial discretization can be eliminated by appropriately selecting a value of k_h that ensures the smoothing length is kept constant as the discretization (or the initial interparticle distance Δ) changes. Thus, if the theoretical shear band thickness is known a priori, the smoothing length can be selected to accommodate this thickness.

For purposes of validation of the constitutive model and as a demonstration of SPH's non-local properties, three different fault rupture simulations are performed, varying the level of discretization while keeping the smoothing length h fixed, modeled after and compared against the centrifuge experiments reported in Anastasopoulos and co-authors' Test 3 and their accompanying FEM simulations [6]. In their experiment, the hanging wall was displaced a total amount of U=1 m at a fault dip of $\theta=60^{\circ}$. For the setup of a similar test, the reader is pointed to the schematic in Figure [3]. The sand in the experiment consisted of medium-dense Fontainebleau sand with $\phi_{\rm max}=39^{\circ}$, $\phi_{\rm res}=30^{\circ}$, $\psi_{\rm max}=11^{\circ}$, $\psi_{\rm res}=0^{\circ}$, $\delta x_f=3.1$, $\delta x_{\rm max}=1.5$, and $\gamma_{\rm max}^p=0.055$. To account for the centrifuge scaling [81], the second term in Eq. [18] must be multiplied by the centrifuge scaling factor (the centrifugal acceleration) n, which equaled 100 in this example.

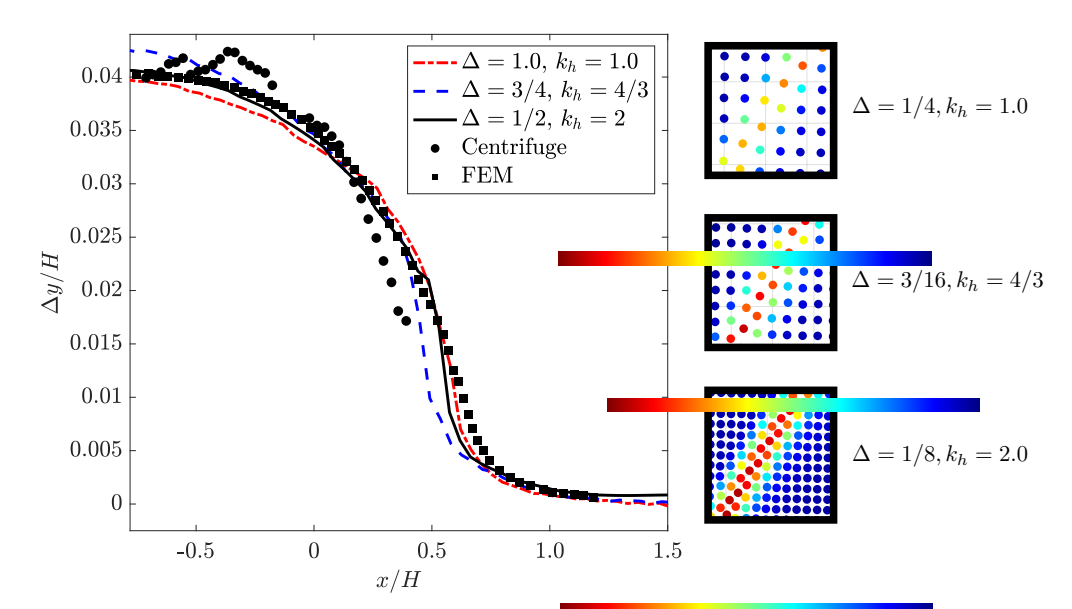


Fig. 1. Vertical displacement Δy normalized by the model height H for three SPH simulations with different levels of particle discretization, while maintaining the smoothing length h fixed compared to centrifuge and FEM results. On the right hand side, screenshots of the propagating shear band at mid-height H/2, for each SPH simulation.

In Figure 1, the vertical displacement of the top ground surface is compared for each level of discretization, as well as with the centrifuge experiments and FEM simulations of 6. The width of the shear bands generated by each of the different discretizations is determined using the method proposed by Rattez et al. 62 where the thickness of the shear band in each coordinate direction k=x,y is defined as the full width at half maximum of a Gaussian function fitted to the accumulated plastic strain, $w_k = 2\sqrt{2\ln(2)}\sigma_k$, where σ is the standard deviation of the Gaussian. The width of the shear band w is then taken from the contributions in each direction,

$$w = \frac{w_x w_y}{\sqrt{w_x^2 + w_y^2}},\tag{21}$$

and the final shear band width is determined as the average of three different measurement locations along the band. For the simulation with $\Delta=1/4$ and $k_h=1$, w=0.495 m, for $\Delta=3/16$ and $k_h=4/3$, w=0.485 m, and for $\Delta=1/8$ and $k_h=2.0$, w=0.483 m. These widths are very close to each other and compare favorably to the experimental shear band width expected from the centrifuge experiments $d_B n=16d_{50}n=0.48$ m, where $d_{50}n=30$ mm is the scaled mean grain size [6]. In fact, the combination of the scaling by the non-dimensional parameter ζ coupled with the non-local properties of the SPH method, significantly help reduce the effect of discretization sensitivity in the softening response and in strain localization, particularly when compared to local plasticity formulations in the finite element method.

3.3 Modified Cam Clay (MCC) model

Introduced by Roscoe and Burland in 1968 [66], the Modified Cam Clay model (MCC), built on the original Cam Clay model introduced at the University of Cambridge, is well suited for modeling normally consolidated or overconsolidated soft clays. In the model, strain hardening and softening are accounted for in the basic formulation without any need for modification or improvement. By virtue of the the critical state line concept, the model is able to distinguish yielding of the material from ultimate collapse.

Through the nonlinear dependence of the void ratio on the pressure and making use of the concept of the state boundary surface, a yield surface can be defined in e-p-q space, where e is the void ratio, $p = \text{tr}[\boldsymbol{\sigma}]/3$ is the mean pressure, and $q = \sqrt{3/2} \|\boldsymbol{s}\|$ is the von Mises (deviatoric) stress, with $\boldsymbol{\sigma}$ the Cauchy stress tensor, and $\boldsymbol{s} = \boldsymbol{\sigma} - p\mathbf{1}$ the deviatoric stress tensor.

In p-q space the yield function for the MCC model is an ellipse given by

$$\mathcal{F} = \frac{q^2}{M^2} + p(p - p_c) \le 0, \tag{22}$$

where the preconsolidation pressure $p_c < 0$, determines the diameter of the ellipsoid in the p-axis. At critical state, the material does not dilate nor compact under shear and the set of points satisfying this condition is given by the critical state line (CSL), taking the form q = -Mp, where its slope, M, is defined as,

$$M = \frac{6\sin\phi_{cs}}{3 - \sin\phi_{cs}},\tag{23}$$

and where ϕ_{cs} is the critical state internal friction angle of the material. The value of ϕ_{cs} is determined for soils from their shear strength under isochoric plastic deformation. The CSL can be considered analogous to a limiting failure envelope for frictional materials, like in the Drucker-Prager criterion. An associative flow rule is used and the plastic deformation rate d^p is expressed as,

$$\boldsymbol{d}^{p} = \dot{\lambda} \frac{\partial \mathcal{F}}{\partial \boldsymbol{\sigma}} = \frac{1}{3} (2p - p_{c}) \mathbf{1} + \sqrt{\frac{3}{2}} \frac{2q}{M^{2}} \hat{\boldsymbol{n}}, \tag{24}$$

where λ is the plastic multiplier and $\hat{n} = s/\|s\|$. The validity of the associative flow rule is supported by experimental evidence, especially on the compression side of the MCC yield surface $\boxed{10}$. In the MCC model, the yield surface expands on the compression side leading to material hardening, whereas it contracts (softens) on the dilation side, and the size for the yield surface is fixed at critical state (see Figure $\boxed{2}$). Because the preconsoldation pressure p_c determines the yield surface diameter, the hardening law determining the expansion or contraction of the yield surface can be formulated in terms of p_c . To time integrate the rate form constitutive equations, a return mapping based on the closest point projection (CPP) algorithm similar to that proposed by Borja and Lee $\boxed{8}$ is used. For details on the implementation of the MCC model within SPH, the reader is referred to $\boxed{25}$.

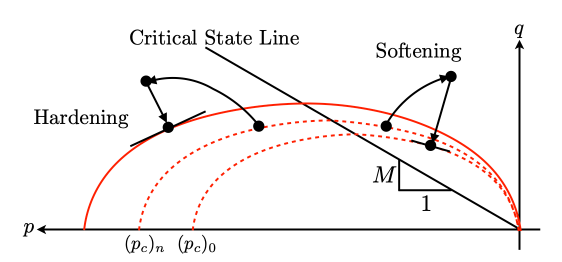


Fig. 2. Modified Cam-Clay plasticity model and yield surface evolution under hardening and softening. Evolving yield surfaces shown in red. The notion of the closest point projection algorithm is shown, with the trial elastic predictor stress returning to the closest point on the yield surface.

3.4 Fault Propagation Simulation Model Setup

Thirteen (2D) plane strain simulations of reverse fault rupture in bedrock overlain by layered soft rock, loose sand or soft clay, and loose sand units (from the lower-most layer to the top-most one, respectively) are performed in a 300-m-wide (L) and 80-m-high (H) computational domain discretized into 24,000

domain particles delimited by walls discretized into boundary particles (see the setup schematic in Figure 3). In eleven of the total simulations, the fault is oriented at $\theta = 60^{\circ}$, whereas in another two, it is oriented at $\theta = 30^{\circ}$. The fault is always embedded in the rigid bedrock simulated by boundary particles. Fault slip is simulated by applying a velocity V on all the boundary particles surrounding the hanging wall side of the fault at the same inclination of the fault in the bedrock. The pushing rate was chosen to be V = 0.5 m/s, such that the loading is quasistatic and the simulations avoid unwanted dynamic effects intrinsic to the SPH method, since the equivalent strain rates sustained throughout the computational domain were considerably lower than the 0.1 s^{-1} threshold at which SPH is known to exhibit certain numerical rate-dependent behavior 79. At the same time, the chosen pushing rate was within the typical range of average fault slip velocities, 57. The pushing (or fault slip) is applied on the hanging wall boundary particles, until the vertical displacement of the hanging wall side U (or fault throw) reached 68% of the total height of the model (U/H = 68%). Additional simulation parameters are provided in Table 1.

Prior to any fault slip, and the initiation of the simulation, the initial stress state is determined throughout the soil deposit. The initial stress state is vital in geotechnical and geosciences applications, and especially so for the MCC model as the soil must be normally consolidated or overconsolidated, and the elastic moduli depend on the pressure p. In our simulations, the stresses are first initialized using the K_0 method, with the relation $K_0 = 1 - \sin \phi_{cs}$, and afterwards a gravity loading is applied in conjunction to a damping term such that the particles comprising the soil deposit reached a state of geostatic stress, that is, the particles were at equilibrium (in terms of a minimum kinetic energy) under gravity load. This initialized geostatic stress state was used in the model where we performed the faulting simulations. In the simulations employing the MCC model, a value for the initial preconsolidation pressure $(p_c)_0$ of each particle is selected. The preconsolidation pressures are determined by assuming a distribution with depth of the overconsolidation ratio, given by,

$$OCR = \frac{(p_c)_0}{p_0} = f(y)$$
 (25)

where p_0 is the initial mean pressure of the soil, determined at the end of the stress initialization procedure. In the simulations, a distribution of OCR ratio decreasing with depth (f(y)) and converging to (but not reaching) that of a normally consolidated soil, OCR= 1, is used, unless otherwise specified (see Figure 23 for the exact depth distribution). Note, the soil was always overconsolidated in our simulations.

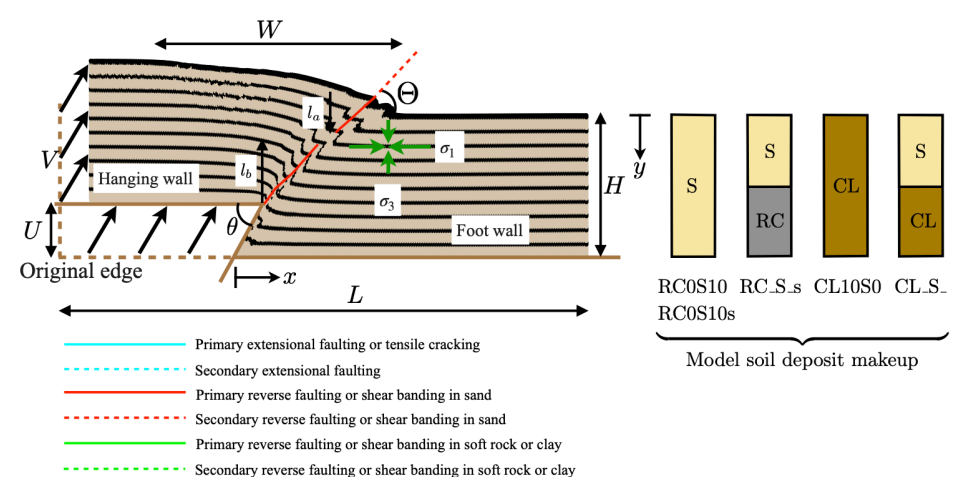


Fig. 3. (left) Schematic showing the setup for the fault propagation simulations. The colored marker layers are for visualizing the deformation patterns and carry no mechanical significance. (right) Soil type makeup of the soil deposits comprised of loose sand (S), soft rock (RC), or clay (CL) in the different simulation types.

Table 1. SPH simulation parameters

Parameter	Value
Time step Δt [s]	0.0024
Initial inter-particle distance Δ [m]	1.0
Smoothing length factor k_h	1.5
Artificial viscosity parameters α_{π} and β_{π}	0.2 and 0.0
Artificial stress parameter ϵ	0.2
Damping coefficient ξ (initialization only)	0.01
Pushing rate V [m/s]	0.5
Height, H [m]	80.0
Length, L [m]	300.0
Bedrock fault orientation angle θ [°]	60 or 30

In eleven of the simulations performed, different layering combinations of loose sands overlying soft clays or soft rock above bedrock were considered at a bedrock fault orientation of $\theta = 60^{\circ}$. Two additional simulations briefly focused on analyzing the effects of changing the bedrock fault angle θ from 60° to 30°. In the simulations, the loose sands were modeled with the Drucker-Prager criterion with either perfect plasticity or using strain softening behavior. The soft rock, corresponded to a weak sandstone rock was always modeled using strain softening behavior. Meanwhile the soft clay was modeled with the Modified Cam Clay formulation previously described in section 3.3. The first simulation denoted RC0S10 consisted of a homogeneous perfectly plastic loose sand layer (called -S for sand) overlying the bedrock (denoted -RC for rock). A nearly identical simulation, RC0S10s added isotropic strain softening behavior (with a -s at the end to denote the softening) to the loose sand. A third simulation denoted CL10S0, was composed of a homogeneous layer of soft clay (denoted -CL for clay) overlying the bedrock, modeled by the MCC model. Eight additional simulations varied the thickness of the soft clay-loose sand strata, and of the soft rock-loose sand strata with the loose sand overlaying the soft clay and soft rock. The simulation names are chosen to incorporate the ratio of layer thickness, e.g., CL3S7 was comprised of a bottom 30% soft clay and top 70% loose sand. In the soft rock-loose sand simulations, strain softening behavior was added to both the soft rock and loose sand hence a -s is added to the end of the simulation name. This -s is omitted from the soft clay-loose sand simulations, since all these incorporated strain softening in the sand. The parameters of the particular materials used in the simulations are compiled in Table 2. In the simulations, the emerging faults and shear band in the soil deposit are labeled -F or -SB, respectively, followed by a particular number and then by the material in which they form. We differentiate between shear bands and faults in the soil deposit based on whether the bands of strain localization are accompanied by any noticeable offsets (discontinuities) in the marker layers across the zone of localized strain. Hence, faults are considered those exhibiting noticeable offset in the markers along the zone of localized strain.

Table 2. Constitutive parameters for the different soil types. Note RC stands for soft rock, S stands for loose sand, and CL stands for soft clay.

Parameter	RC	\mathbf{S}	\mathbf{CL}
Initial density ρ [kg/m ³]	1570	1590	1600
Peak internal friction angle, ϕ_{max} [°]	43.6	37	_
Residual internal friction angle, $\phi_{\rm res}$ [°]	39.8	34.7	_
Peak dilation angle, ψ_{max} [°]	37.6	12.8	_
Residual dilation angle, $\psi_{\rm res}$ [°]	0	0	_
Threshold octahedral plastic strain, γ_f^p	0.013	0.022	_
Cohesion, c [kPa]	143	0	_
Young's Modulus, E [MPa]	218.9	20	_
Poisson Ratio, ν	0.3	0.3	0.3
Initial OCR ratio,	f(y)	f(y)	f(y)
Critical state line slope, M	_	_	1.45
Initial void ratio, e	_	_	0.7
Virgin isotropic consolidation index, λ	_	_	0.355
Swelling index, κ	_	_	0.0477

In what follows a few terms and definitions are introduced. The width of the region of flexure, i.e., the region where the surface has been distorted by the propagating fault, spanning from the furthermost synthetic (i.e., dipping in the same direction as the bedrock fault) fault rupture on the foot wall side to the point on the hanging wall side where the monocline hinge is located (see Figure 3), is denoted the surface distortion zone W. On the hanging wall side, it may also be delimited by the furthermost antithetic (i.e., dipping in the direction opposite that of the bedrock fault) extensional fault, or tension crack, should these form. To quantify the progress of fault growth and propagation through the soil deposit, we measure the vertical height of the fault. However, in our simulations, the faults on occasion do not propagate as a continuous section, and instead form in segments, propagating from both top and bottom of the soil deposit and coalescing at the interface boundary between both soil types within the soil deposit. Hence, we measure the total vertical height of the fault l as the sum of the height of the fault segment from above, l_a , with the height from the segment from below, l_b . Lastly, the vertical component of the slip of the bedrock fault is denoted as U, and is alternatively called the fault throw, or the vertical bedrock fault displacement due to the manner in which the fault slip is imposed.

4 Fault rupture in stratified soil

4.1 Single layer models

Figure 4 shows the results of the RC0S10 simulation containing homogeneous perfectly plastic loose sand. In the top row, contours of the accumulated plastic strain ε_{acc}^p are plotted in conjunction with deformed colored marker layers on the right-hand side, both evaluated at U/H=40%. The marker layers are purely for purposes of visualization of the deformation patterns. From the deformed marker layers and the accumulated plastic strain, three distinct faults, RC0S10-F1, RC0S10-F2 and RC0S10-SB1, can be distinguished. Note that in these models, antithetic shear banding or faulting, shown in cyan color, forms in addition to synthetic bands or faults.

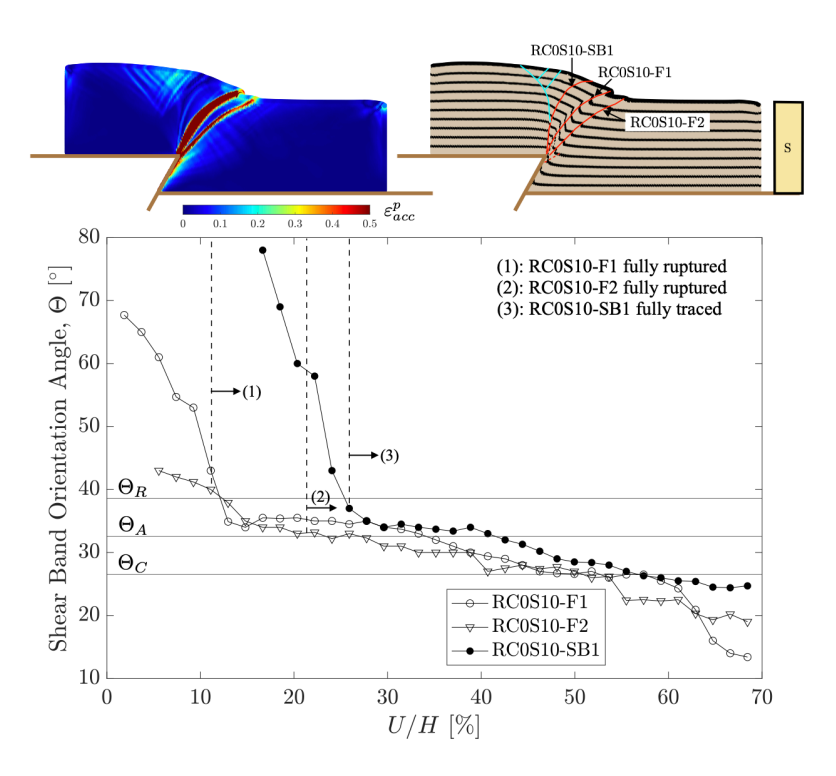


Fig. 4. Evolution of shear band and fault orientations measured at their upmost tip for the RC0S10 simulation (perfectly plastic sand). Θ_R , Θ_A , and Θ_C , are the theoretical measures of the Roscoe, Arthur and Coulomb angles respectively. At the top, contours of the accumulated plastic strain ε_{acc}^p are shown on the left and deformed colored layers are shown on the right for the RC0S10 simulation at U/H = 40%. The column to the right of the deformed colored layers depicts the soil deposit makeup.

A few structural observations common to the majority of the fault propagation simulations can be drawn. For example, once the first fault ruptures the soil deposit surface, a small local step in the ground surface appears, corresponding to the fault scarp. As slip on the fault continues to accumulate (i.e., over further vertical displacement of the hanging wall side) the soil surface deforms through flexure, and a gently rolling monocline develops as the main structural feature. In all simulations, the deformation generated from the fault in the bedrock progressively opens up towards the surface spanning a relatively wide zone which may encompass more than one fault or shear band. The particular fault or shear band decreases in dip towards the top ground surface, and ruptures further along the foot wall side than would a direct extension of the fault plane from the bedrock fault. At the surface, the extent of the region where the surface has been significantly distorted by the propagating fault is known as the surface distortion zone W, and is delimited by the antithetic (cyan) and the main synthetic through-going faults or shear bands (red).

In the main panel of Figure 4 the orientation history of the shear bands and faults as a function of normalized fault throw (U/H) for the RC0S10 simulation is displayed. Fault RC0S10-F1 ruptures at the surface first around U/H = 10.5% with an inclination slightly greater than that of the theoretical Roscoe angle prediction. Fault RC0S10-F2 which begins propagating shortly after fault -F1 ruptures at the surface at U/H = 21.5% taking a somewhat shallower inclination closer to the Arthur angle prediction. Lastly, the shear band RC0S10-SB1 which emanates slightly left of the corner of the bedrock and follows a steep trajectory exclusively on the hanging wall side, rupturing at a steepness slightly below the Roscoe prediction. Over continued accumulated fault throw U/H, the faults and shear bands rotate their orientation towards the Arthur prediction then the Coulomb angle, and then towards even shallower orientations. A rapid decrease in steepness precedes the eventual surface rupture of the faults or shear

14

bands, and then the faults and shear bands quickly leave the Roscoe orientation to stabilize at the Arthur angle, roughly from around U/H = 13 to 45%, depending on the particular fault or shear band, before continuing rotation towards the Coulomb angle or shallower inclinations.

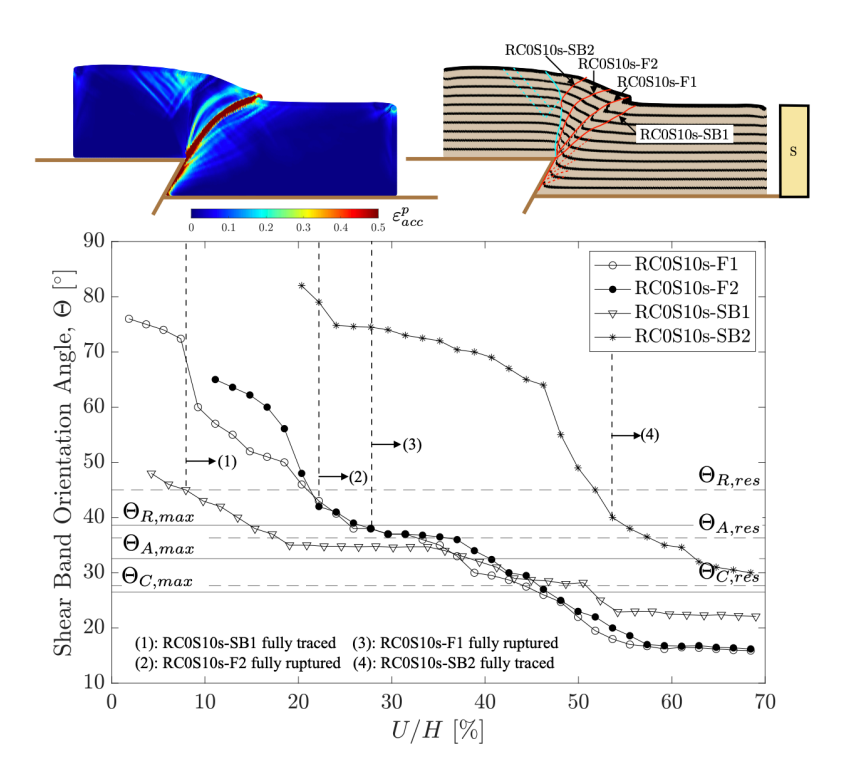


Fig. 5. Same as Figure 4 but for the RC0S10s simulation (sand with strain softening). Note $\Theta_{R,max}$, $\Theta_{A,max}$, and $\Theta_{C,max}$, are the theoretical measures of the Roscoe, Arthur and Coulomb angles respectively using the peak friction and dilatancy angles, whereas $\Theta_{R,res}$, $\Theta_{A,res}$, and $\Theta_{C,res}$ are determined with the residual values.

In the results shown in Figure 5 for the RC0S10s simulation, strain softening behavior is added to the plasticity model for the loose sand. Again, in the top row of the figure, contours of ε_{acc}^p are shown on the left and the colored marker layers on the right at U/H = 40%. The strain softening behavior encourages further localization, generating an additional shear band on the hanging wall side compared to the perfectly plastic RC0S10 simulation. The first shear band or fault to rupture at the surface is RC0S10s-SB1, taking an initial orientation almost exactly at the Roscoe prediction using the residual values of friction and dilatancy ($\Theta_{R,res}$), and the second fault to propagate, RC0S10s-F1, does so at an angle slightly shallower than $\Theta_{R,res}$. The next two surface ruptures that follow take an initial orientation close to the $\Theta_{R,max}$ prediction calculated with the peak friction and dilatancy angles. While the stability period at the Arthur angle is reduced somewhat in duration, the overall Roscoe to Arthur to Coulomb rotation is still observed in the shear bands and faults, regardless of the presence of strain softening behavior.

A marked difference between the RC0S10 and RC0S10s simulations is that in the former, the first zone of localized strain to propagate through the soil deposit possesses significant lateral offset across the trace of the localization zone. For this reason, it is considered to be a fault (-F) and denoted RC0S10-F2, whereas in the simulation with softening behavior, the lateral offset is absent across the same first localized strain region to fully propagated, and is denoted as a shear band (-SB) as RC0S10s-SB1. The additional shear band on the hanging wall side in the RC0S10s simulation, compared with RC0S10, is likely a product of the addition of strain softening. The larger magnitude of the plastic strains accumulated along the

bands on the hanging wall side, compared to those which are closer to the foot wall side, may contribute to the negligible amount of offset across RC0S10s-SB1, as slip from the bedrock fault is accommodated elsewhere.

Figure $\boxed{6}$ depicts the evolution of shear band and fault orientations for the CL10S0 simulation, consisting of a homogeneous soft clay deposit modeled with the MCC model. A few salient features are distinct with respect to the loose sand simulations. For example, all the shear bands or faults either form in the middle shear zone between hanging wall and foot wall, or on the foot wall side. Instead of multiple fault surface rupture locations, only one localized fault ruptures at the surface, despite there being a similar relatively wide shear zone through the middle of the soil deposit. In addition, because the MCC model is able to capture yielding in compression, a small lobe of plastic strain accumulates at the bottom of the hanging wall side near the fault tip in the bedrock. Furthermore, because of significantly large tensile σ_{xx} stresses near the monocline hinge at the top surface, a tensile crack opens around U/H = 33% continuing to propagate for the duration of the simulation. The considerable material strength due to the highly overconsolidated nature of the soil near the top surface, prevents any lateral spreading of the soil or extensional faulting and instead aids in concentrating the deformation into singular cracks. Such tensile cracks are commonly observed in analogue models of clays or cohesive soil $\boxed{38}$, $\boxed{77}$, as well as in the field $\boxed{60}$, and form on the hanging wall sides of the fault, tending to widen with increased slip of the bedrock fault $\boxed{4}$.

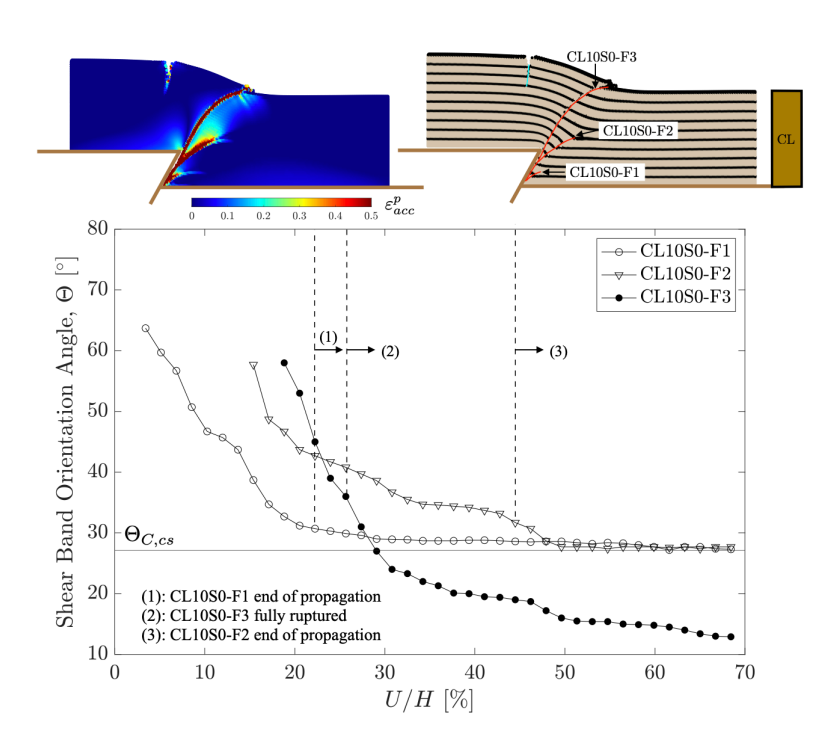


Fig. 6. Evolution of shear band and fault orientations measured at their upmost tip for the CL10S0 simulation (soft clay modeled with the MCC). $\Theta_{c,cs}$ constitutes the theoretical Coulomb angle employing the critical state friction angle ϕ_{cs} . At the top, contours of the accumulated plastic strain ε_{acc}^p are shown on the left and deformed colored layers are shown on the right for the CL10S0 simulation at U/H = 40%

In the perfectly plastic or softening enhanced Drucker-Prager models of loose sand, with the exception of a few secondary shear bands, the majority of the faults which form all eventually rupture at the surface. This not the case for simulation CL10S0, with faults rupturing through soft clay, as the first two faults to develop (CL10S0-F1 and CL10S0-F2) fail to reach the top ground surface. These two ruptures initially

take an orientation close to $\Theta = 60^{\circ}$ and rapidly shallow until the fault ceases propagating and swiftly reaches an orientation consistent with the Coulomb angle ($\Theta_{C,cs}$) calculated using the critical state friction angle ϕ_{cs} that defines the CSL line of the MCC model. As the fault shallows, the amount of vertical slip that can be accommodated per the amount of horizontal soil stress that must be overcome to continue propagating at a shallow angle, renders the rupture energetically unfavorable and thus a new steeper rupture is induced on the hanging wall side of the existing rupture. Nevertheless, we notice that the faults do continue to grow slightly longer after the new rupture has formed on the hanging wall side of the previous rupture, not ceasing to propagate abruptly once the new rupture emerges.

Since faults CL10S0-F1 and CL10S0-F2 stay on the foot wall side of the final through-going fault which ruptures at the surface (CL10S0-F3) eventually obtaining the fixed orientation of $\Theta_{C,cs}$ once their propagation process reaches completion and do not undergo a further rotation, this strongly suggests that the rotation of CL10S0-F3 is at least partially the result of a rigid body rotation. Once fault CL10S0-F3 is fully propagated through the soil deposit, more slip is accumulated on the bedrock fault and due to the increasing warping near the top ground surface as the monocline develops, the fault lying through this zone of the soil will likewise be warped. Because of the absence of the dilatancy parameter from the MCC model, we note that the Roscoe and Arthur theoretical orientations cannot be determined for faults or shear bands rupturing through the soft clay deposit.

A withstanding question is whether the shear bands or faults which initially form at orientations close to 60° in the CL10S0 simulation or greater like in the RC0S10s and RC0S10 simulations, do so as a direct consequence of the fault dip in the bedrock $\theta = 60^{\circ}$, or due to the mechanical properties of the soil layer. To test the influence of the fault dip in the bedrock on the shear band or fault orientation in the soil deposit, two additional simulations are performed with a fault dip of $\theta = 30^{\circ}$. These simulations, CL10S0- θ 30 and RC0S10s- θ 30, consist of 100% clay and loose sand respectively and the evolution of the shear band and fault orientations of each are shown in Figures 7 and 8.

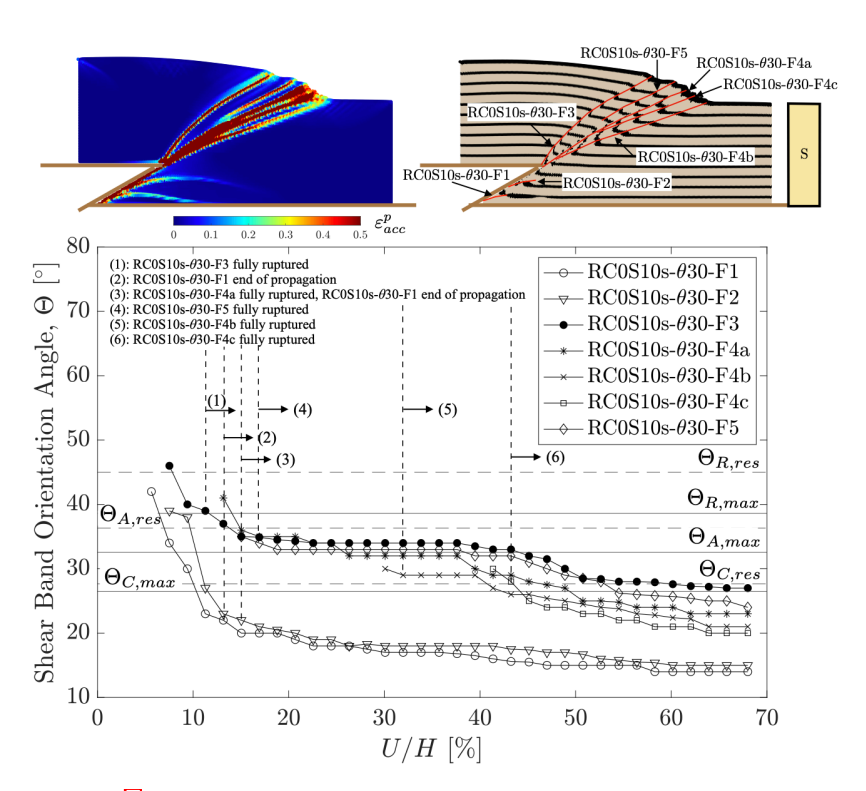


Fig. 7. Same as Figure 4 but for the RC0S10s- θ 30 simulation (sand with strain softening) and $\theta = 30^{\circ}$.

For the CL10S0- θ 30 simulation and RC0S10s- θ 30 simulation, the initial orientation taken by the faults is around 40° to 50°, which is a noticeable decrease from the roughly 60° of the simulations with $\theta = 60^{\circ}$. However, in the RC0S10s- θ 30 simulation the angle at which the fault is fully ruptured (surface rupture angle) is still close to the Roscoe angle given the peak dilatancy angle $\Theta_{R,max}$ as seen in the previous $\theta = 60^{\circ}$ simulations. This result suggests that the surface rupture angle is considerably less dependent on the bedrock fault orientation angle than is the initial fault or shear band orientation in the soil deposit.

A few other features are noted. Changing the bedrock fault angle to 30° in the CL10S0- θ 30 simulation has the effect of deterring localization and requiring a substantially larger amount of bedrock displacement for the fault to be fully ruptured across the soil deposit. Also, the bands forming in the foot wall side rotate slightly past the critical Coulomb orientation ($\Theta_{C,cs}$), likely due to the additional horizontal compression coming from the shallower bedrock fault angle. In addition, the smaller bedrock fault angle has the effect of extending the period of relative fault orientation stability around the Arthur angle in the RC0S10s- θ 30 simulation.

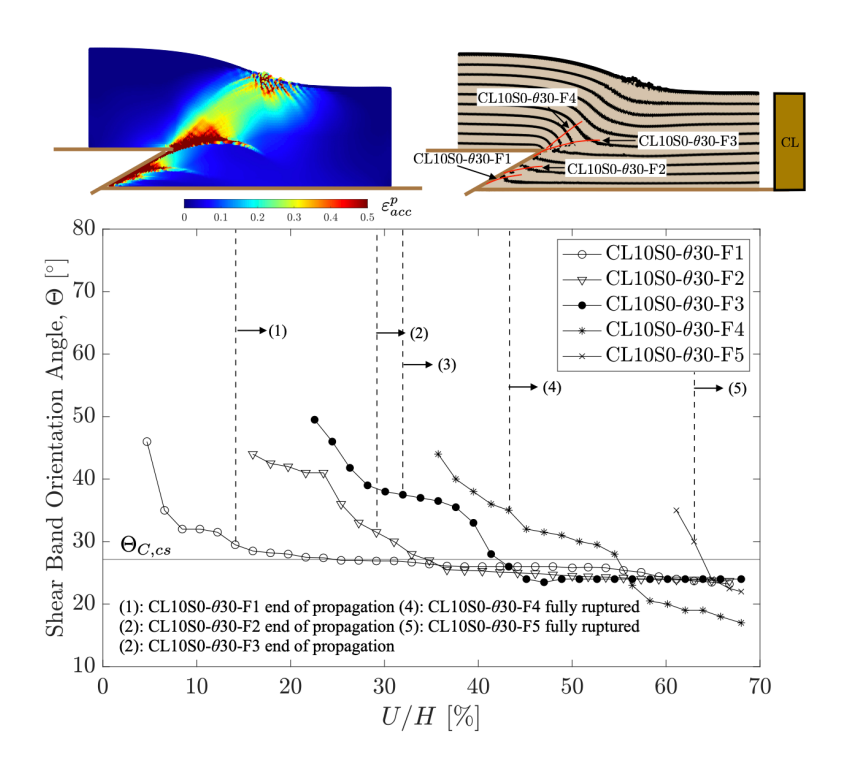


Fig. 8. Evolution of shear band and fault orientations measured at their upmost tip for the CL10S0- θ 30 simulation (soft clay modeled with the MCC) with bedrock fault orientation of $\theta = 30^{\circ}$. At the top, contours of the accumulated plastic strain ε_{acc}^p are shown on the left and deformed colored layers are shown on the right for the CL10S0 simulation at U/H = 40%. A fifth fault RC0S10s- θ 30-F5 emerges at U/H = 62% and is therefore not visible in the screenshots at U/H = 40%.

In Figure 9 and 10 the directions of σ_1 and the deviation of this direction from the horizontal quantified by the angle α are plotted in Panel (a). Likewise, polar histograms of $|\alpha|$ and $|\beta|$ (Panel (b)), where β is the deviation of the direction of the principal strain increment (d_1) from the horizontal, and of the degree of coaxiality (Panel (c)) are shown. The extensive horizontal compression in the $\theta = 30^{\circ}$ simulation can be seen by the direction of both the maximum principal stress and strain increment in Panel (b). In the shear zone where the fault ruptures, both directions are roughly horizontal. The $\theta = 60^{\circ}$ (Figure 9) differs in this regard, being slightly less coaxial as seen in Panel (c). Overall, however, the directions of maximum principal stress and strain increment are mostly aligned with each other, especially in the

18

fault rupture shear zone indicating that measuring the fault orientations with respect to σ_1 is a correct approach.

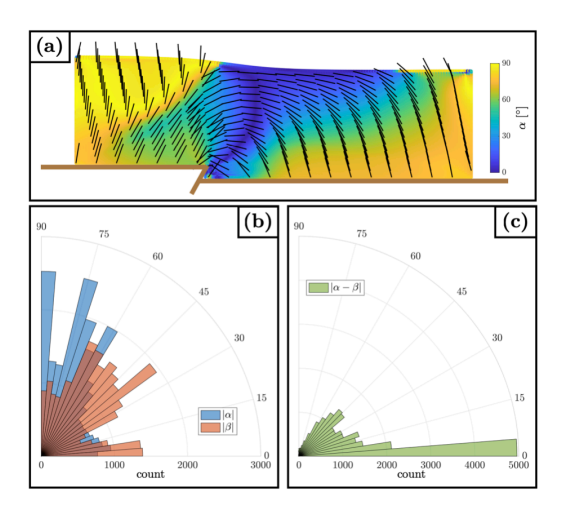


Fig. 9. Panel (a) shows contours of deviation angle α of the direction of σ_1 from the horizontal with vectors indicating the σ_1 direction superimposed for simulation CL10S0 at U/H = 15%. In (b) polar histograms of $|\alpha|$ and $|\beta|$ the deviation of the direction of the maximum principal strain increment d_1 from the horizontal. In (c) a histogram showing the degree of coaxiality $|\alpha - \beta|$ is plotted.

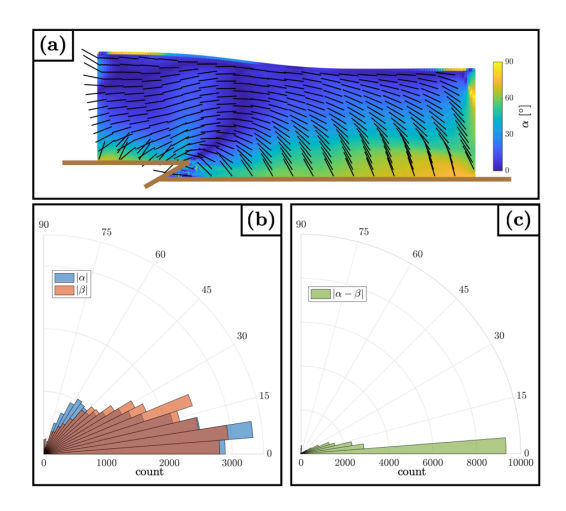


Fig. 10. Same as Figure 9 but for the CL10S0- θ 30 simulation, that is with bedrock fault inclination of $\theta = 30^{\circ}$.

4.2 Multilayer models

In Figure 11, the visualizations of the eight different multilayer simulations are shown at U/H = 40%. Simulations RC3S7s to RC9S1s on the left side of the figure, increase the proportion of bottom soft rock

relative to top loose sand (with softening) from 3:7 to 9:1. The right hand side plots do the same with simulations ranging from CL3S7 to CL9S1 changing the ratios of soft clay to loose sand (with softening). Varying the height of the soft rock-sand or clay-sand layers has a profound impact on the number of faults and shear bands which propagate across the main synthetic shear zone, and also extend the number and depth of secondary antithetic faults or, in the case of simulations with clay, tension cracks.

Adding a thin layer of soft rock below the loose sand in RC3S7s reduces the number of through-going faults (RC3S7s-F2aRC/RC3S7s-F2aS and RC3S7s-F2bRC/RC3S7s-F2bRC) with respect to RC0S10s, but the presence of the soft rock foments the nucleation of a fault RC3S7s-F1RC which precedes the main through-going ones, but does not penetrate the soft rock-loose sand interface, similar to fault CL10S0-F1 and fault CL10S0-F2 in the CL10S0 simulation. Likewise, in the RC5S5s simulation, composed of a bottom 50% soft rock and a top 50% loose sand, (see Figure 12 for the evolution of the shear band and fault orientations) the first fault to emerge, RC5S5s-F3RC, stops growing at an orientation close to the Roscoe angle and remains in the soft rock on the foot wall side. By that point, a new rupture (RC5S5s-F1RC) has already emerged on the hanging wall side of RC5S5s-F3RC. As RC5S5s-F3RC shallows, it cannot overcome the horizontal stress to continue propagating, making the RC5S5s-F2RC fault more favorable for growth to account for the continued slip on the bedrock fault.

Fault RC5S5s-F1RC is the first to propagate fully across the soft rock bottom layer, and refracts upon entering the more compliant sand, locally becoming steeper (as fault RC5S5s-F1S). Fault RC5S5s-F1S in the loose sand ruptures at the surface at an inclination steeper than the residual Roscoe dip and continues rotating over increasing slip in the bedrock fault. At around U/H = 20%, a third fault (RC5S5s-F2RC) develops, quickly traversing the soft rock and again refracting into the upper loose sand layer (continuing as RC5S5s-F2aS). Fault RC5S5s-F2aS subsequently performs a rotation towards and past Coulomb orientations. Fault RC5S5s-F2bS which bifurcates from fault RC5S5s-F2aS within the sand layer after fault RC5S5s-F2aS had already ruptured at the surface, does not follow this previous trend, instead forming at an orientation similar to that of RC5S5s-F2aS at that given amount of U/H (i.e., close to $\Theta_{A,max}$). In addition, fault RC5S5s-F2cS also does not follow the Roscoe-Arthur-Coulomb rotation, and instead bifurcates from the tip of fault RC5S5s-F2RC at the soft rock-loose sand interface initially taking an inclination steeper than that of RC5S5s-F2aS and rapidly reaching Coulomb or shallower dips. Overall, in the RC5S5s simulation, a rotation of the shear bands and faults is once again observed, but the presence of the soft rock-loose sand layering significantly reduces the period of orientation stability and the Arthur angle, with a more continuous dip angle obtained closer to the Coulomb angle from U/H = 30to 60%.

In contrast, in the RC7S3s simulation, the first fault to emerge in the now enlarged soft rock bottom layer (RC7S3-F2RC) propagates across the soft rock, entering and rupturing at the top surface of the loose sand layer (as fault RC9s1-F2aS and -F2bS, as the fault bifurcates within the loose sand layer). A similar pattern is seen in the RC9S1s simulation, as the first fault to emerge RC9S1-F1RC which crosses into the sand, continues to rupture first at the surface, and no stunted fault remains in the soft rock layer. In effect, the enlargement of the soft rock layer relative to the sand stratum stymies the formation of stunted faults forming on the foot wall side. The high cohesion of the soft rock layer (143 kPa) helps concentrate the otherwise wide shear zone seen in the models dominated by loose sand. This feature may aid to reign in the first emergent faults and prevent them from rotating towards unfavorable orientations. which would bequest a new, more favorable fault rupture through the soil deposit. Another notable trait of the loose sand layers is the prominence of extensional faulting in the vicinity of the monocline hinge. Both antithetic and synthetic extensional faults near the monocline hinge generally have an orientation close to 60° with respect to the direction of σ_1 which is not far from the peak Coulomb prediction under active loading conditions which is $45^{\circ} + \phi_{\text{max}}/2 = 63.5^{\circ}$. This rule is broken for the furthermost antithetic faults in some simulations such as RC5Ss where the fault further steepens at its tip just prior to rupture in the form of a small nearly vertical tensile crack. As the sand layer depth is reduced relative to the soft rock, the number and intensity of the extensional faulting diminishes, as the monocline slope is reduced due to the increased cohesion in the soft rock.

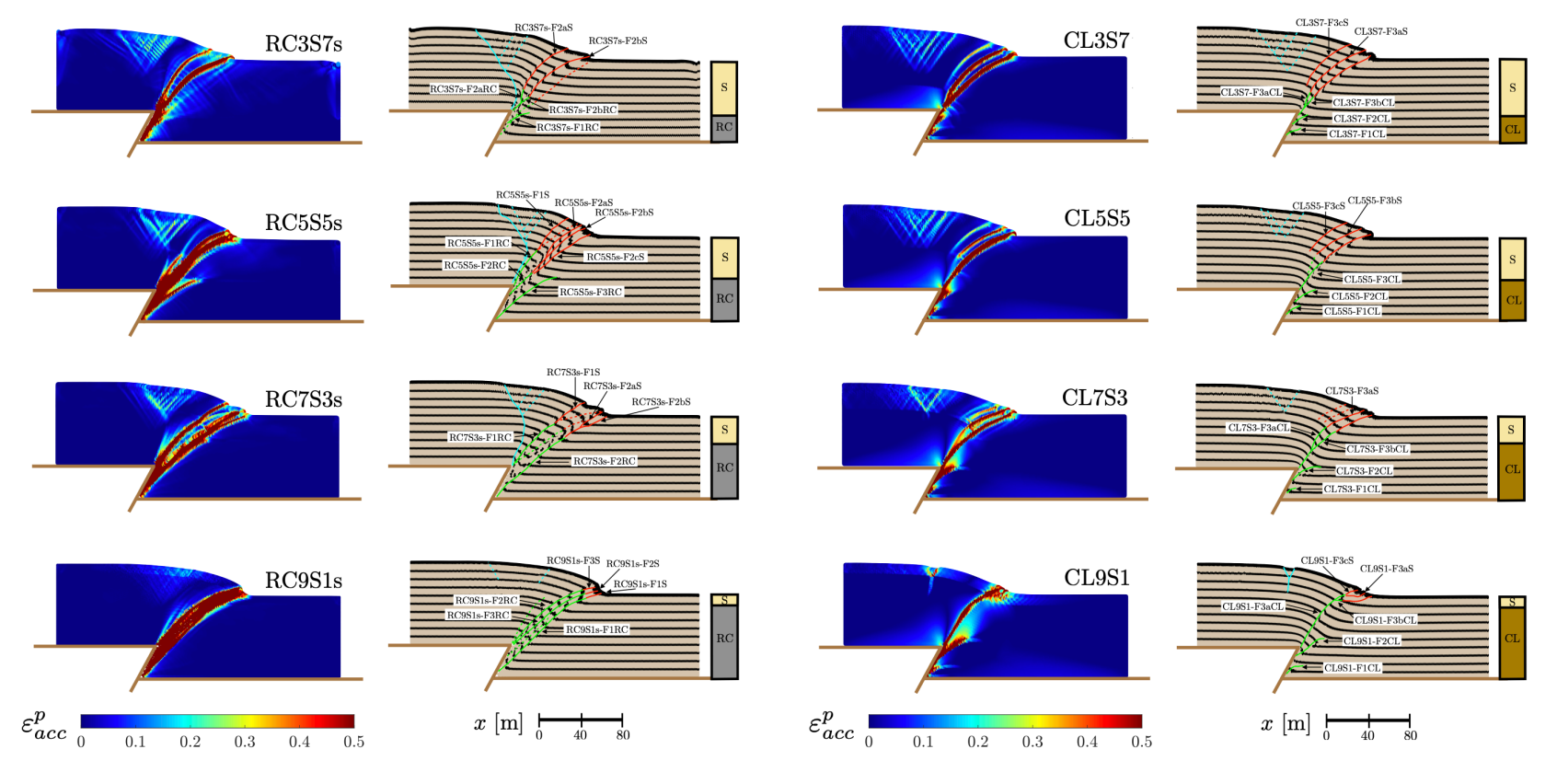


Fig. 11. Visualizations of the accumulated plastic strain ε_{acc}^p contours and deformed colored layers for the soft rock-sand simulations (left two columns) and for the soft clay-sand simulations (right two columns) at U/H = 40%.

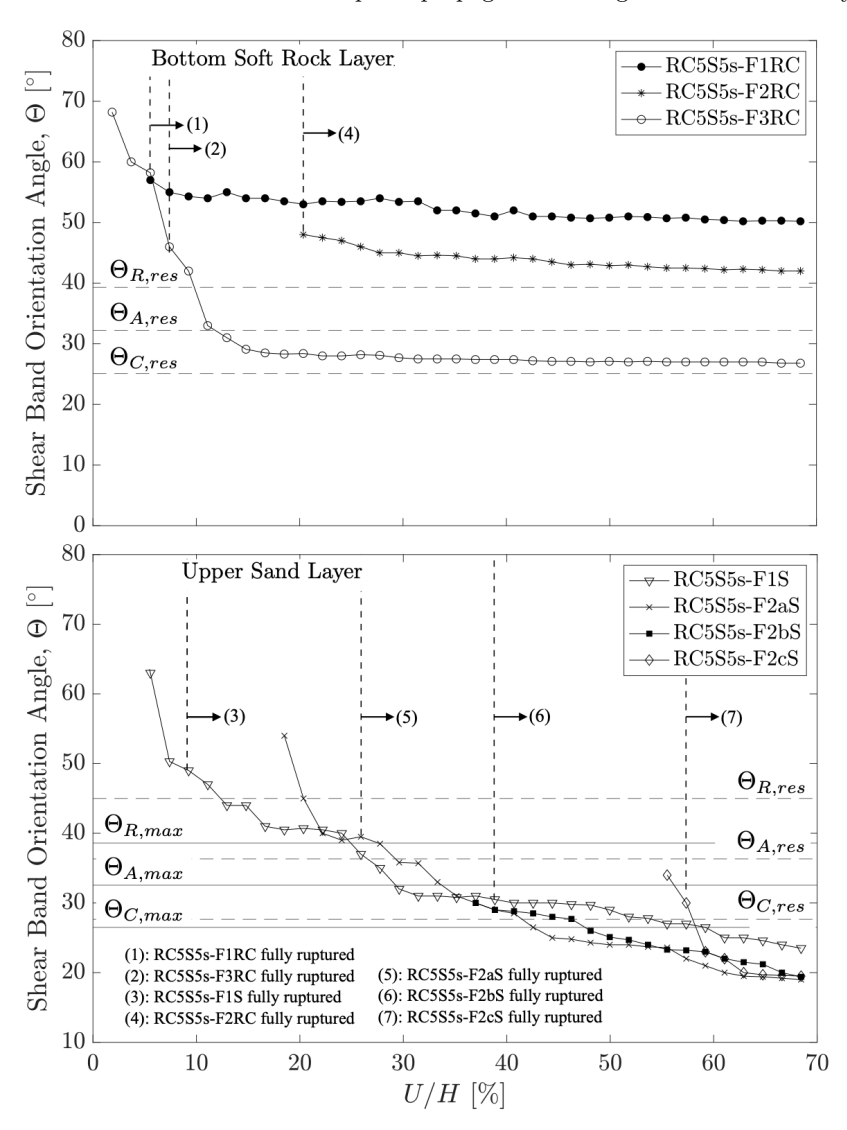


Fig. 12. Evolution of shear band and fault orientations measured at their upmost tip for the RC5S5 simulation. The top panel shows the inclinations in the lower soft rock, while the bottom panel displays them in the upper sand layer. For visualizations of the accumulated plastic strain ε_{acc}^p contours and deformed colored layers, see Figure 11.

In the soft clay-loose sand simulations, depicted on the two right-hand side columns of Figure [11], yielding in compression is observed throughout the simulations at the bottom corner of the hanging wall. In general however, localization of the main shear band occurs first at the top in the loose sand, and then the fault grows from the tip of the fault in the bedrock through the clay to merge with the upper section through the sand. Thus, the direction of propagation is bidirectional from two starting points towards the interior of the soil deposit, which contrasts with the exclusive upwards propagation of the soft rock-loose sand, pure sand or pure soft clay simulations. Since the shear bands do not cross from the bottom into the top layer, they also do not refract and become locally steeper across the interface boundary. Instead, the overall orientation shallows across the interface boundary once the fault propagating through the bottom soft clay is fully ruptured and coalesces with the already-formed segment in the overlying sand. In addition, stunted faults are generated in all simulations along the foot wall, with their ultimate length increasing with the relative thickness of the clay layer with respect to the sand layer. Analogue experiments at 1-g

demonstrated that an increase of clay content in granular soils further predisposed the soil towards similar stunted fault ruptures. Furthermore, the increase in clay content lead to less pronounced fault scarps at the top surface in their experiments, a feature shared with our simulations when the thickness of the clay increases with respect to that of the sand. Lastly, as the thickness of the top sand decreases relative to the clay, conjugate extensional faulting transitions into tension cracking, like in the single clay layer simulation CL10S0, since the extensional faults seen in the sand do not penetrate into the underlying clay. In Figures 13 and 14 the CL7S3 simulation is examined in closer detail, tracking the orientations of the emerging faults and recording the stress history of a number of marker points in the simulation.

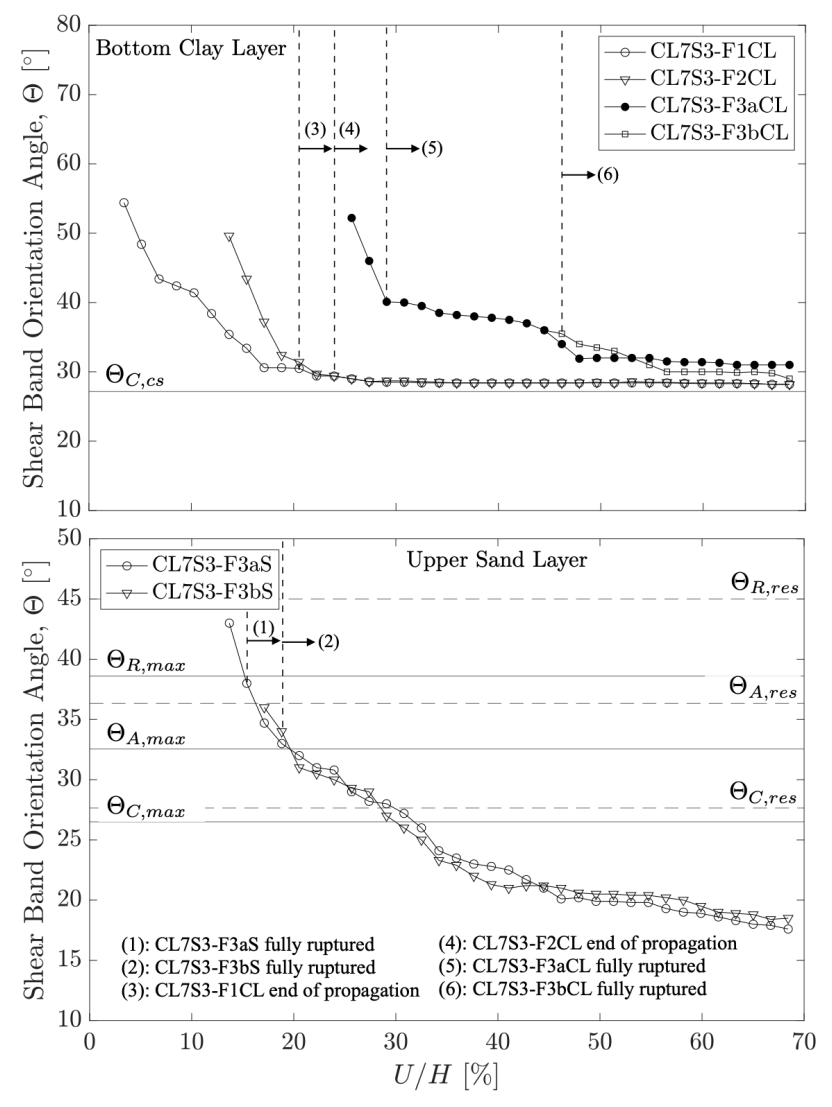


Fig. 13. Same as Figure 12, but for the CL7S3 simulation.

The first fault to emerge in the bottom clay layer, CL7S3-F1CL, fails to propagate through the entirety of the soil deposit and instead rotates into a Coulomb orientation $\Theta_{C,cs}$ given the critical friction angle ϕ_{cs} . Similarly, fault CL7S3-F2CL also ceases to propagate prematurely, remaining in the bottom clay and rotating into a similar inclination of $\Theta_{C,cs}$. Slightly prior to the end of growth for both of these

faults, at around U/H=15% and 18%, faults CL7S3-F3aS and CL7S3-F3bS rupture downwards from the top surface through the top loose sand layer. Here they are joined by fault CL7S3-F4aCL and fault CL7S3-F4bCL which branches off from the later, coalescing at the soft rock-sand interface boundary with the respective fault segments in the sand.

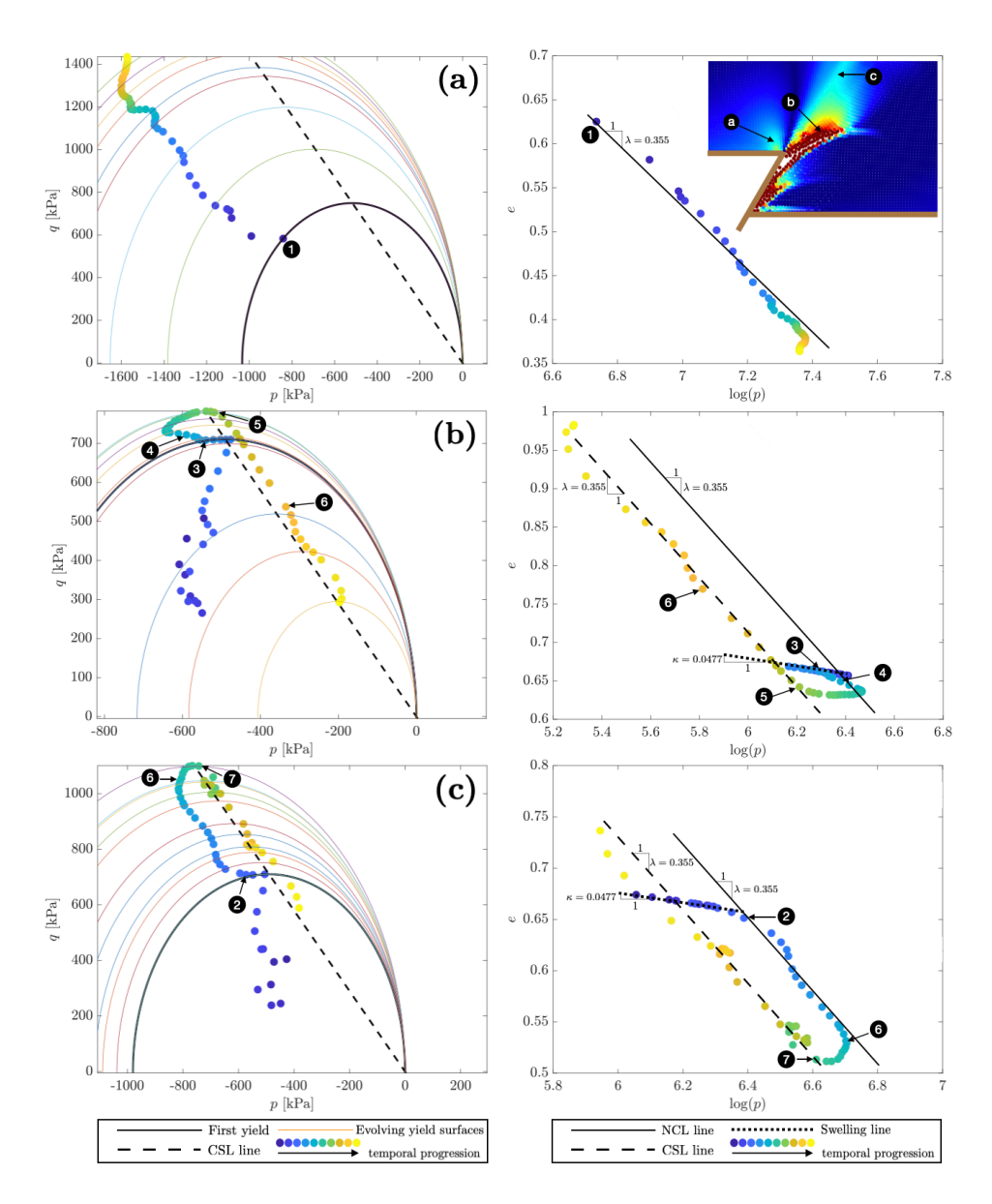


Fig. 14. Stress histories of three different measurement points within the CL7S3 simulation recorded from U/H = 2% to U/H = 30%. The locations of the measurement points (a), (b), (c) are indicated in the inset on the top right hand side panel, showing contours of the accumulated plastic strain. Events of importance noted as (1)-(7) are mentioned in the main text.

Three marker points are selected within the bottom soft clay layer of the CL7S3 simulation, which are shown in the inset in Figure 14. Point (a) corresponds to a particle located just above the bedrock along the hanging wall near the tip of the bedrock fault, in a region experiencing compression-driven yielding.

Point (b) is a particle lying within a stunted fault (the second one to form, CL7S3-F2CL), and point (c) is situated in an area through which the first through-going shear band propagates (CL7S3-F3aCL). Point (a) shows a primarily compressive stress path with some degree of shear in p-q space (left column) despite being a little tortuous towards the end of the trajectory. Yielding occurs on the compression side of the yield surface with initial yielding at time (1), corresponding to U/H = 2% and then progressive hardening follows, augmenting the radius of the yield surface.

Yielding along the main through-going shear zone occurs later with point (c) yielding at U/H = 8.5% and point (b) slightly afterwards at U/H = 9.3%. In $\log(p) - e$ space (left side panels), the material undergoes normal consolidation at this stage, subsequently following the normal consolidation line (NCL). At time (4), fault CL7S3-F2CL begins to grow and ends its propagation at time (5) at U/H = 16.2%, becoming a stunted fault. By time (5), point (b) has reached the critical state line (CSL) and softens, subsequently unloading and following a trajectory parallel to the CSL line in both p-q and $\log(p)-e$ space. The propagation of fault CL7S3-F3aCL initiates at time (6), or U/H = 20%, and by the time it is fully ruptured across the bottom soft clay layer at time (7), with U/H = 28.8%, the material at Point (c) reaches the CSL line, and softens, dilating substantially. The dilative behavior of the stunted faults in stress space agrees with their ultimate orientation in terms of the critical Coulomb angle $\Theta_{C,cs}$, and the shown stress paths highlight the relevance of yielding in compression despite the overall shear motion of the propagating fault, which is only possible thanks to the employment of the MCC model.

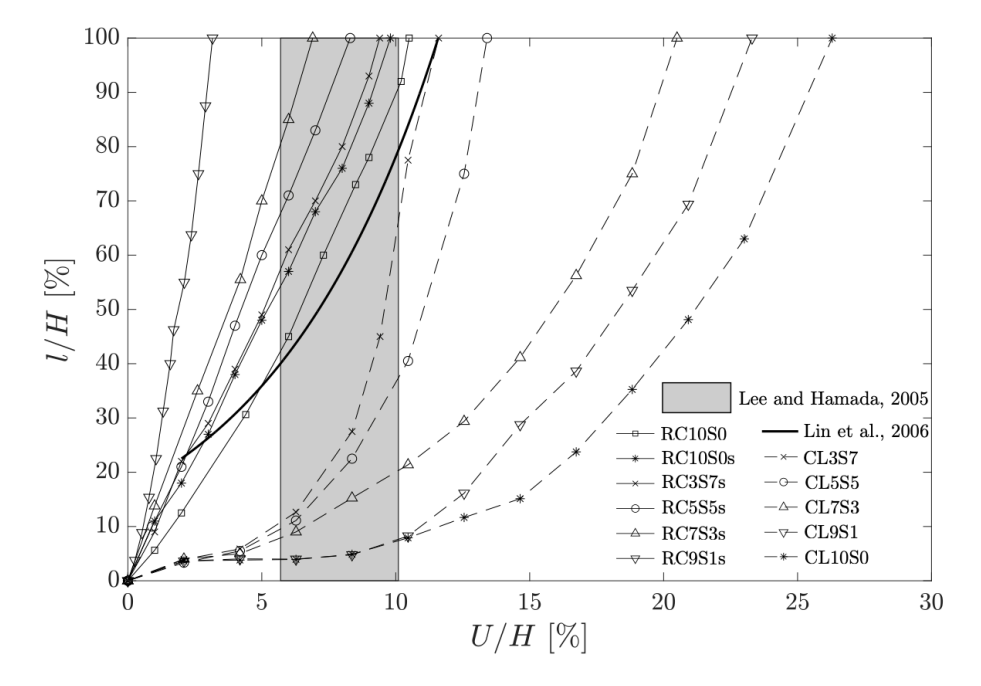


Fig. 15. Evolution of the normalized shear band or fault height with respect to the normalized vertical bedrock displacement for various conducted simulations. Here, l is the cumulative vertical extension of the first throughgoing shear band or fault in each simulation. The shear band or fault extends across the soil layer at l/H = 100% at a critical normalized bedrock displacement of U_{cr}/H .

As the thickness of bottom soft clay relative to the top loose sand increases, the soil deposit behaves in an increasingly ductile manner and is able to "absorb" the bedrock fault slip deformation, delaying the onset of fault rupture. This is manifested by the increased amount of critical vertical bedrock displacement required for the faults to fully propagate through the soil deposit. In Figure 15, the vertical length l of the shear bands or faults that first rupture in each of the simulations performed with a bedrock fault

angle of $\theta = 60^{\circ}$ is tracked in time as a function of normalized vertical fault throw U/H. Note, because in the soft clay-loose sand simulations, the fault ruptures through the top sand first, the total cumulative vertical length l is measured as the combined height from the fault segments in the sand (l_a) and in the clay (l_b) .

While the increasing proportion of clay relative to sand in the soft clay-loose sand simulations augments the normalized critical bedrock displacement U_{cr}/H , in the soft rock-loose sand simulations, an increase in the proportion of the soft rock has the opposite effect, reducing U_{cr}/H . Namely, the more brittle soft rock cannot absorb the displacement imparted by the bedrock fault and the resultant fault rapidly ruptures through the soil deposit. Comparing the results of the two exclusively loose sand simulations RC0S10s and RC0S10, the absence of softening behavior actually enlargens the critical bedrock displacement required for fault rupture through the sand deposit. Such behavior is likely a product of the heightened proclivity towards strain localization introduced by the softening behavior. The critical bedrock displacement of both loose sand simulations agrees well with other analogue experimental [43] and numerical simulations [46] modeling fault rupture through loose sand deposits with similar material parameters.

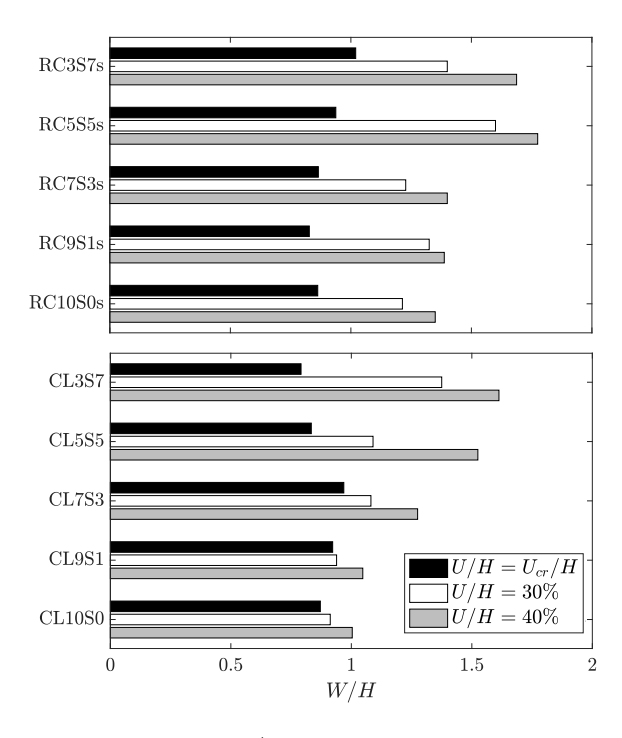


Fig. 16. Normalized surface distortion width W/H at three different values of normalized bedrock displacement.

Figure 16 showcases the extension of surface distortion, measured using a normalized surface distortion width W/H, for the different soft rock-loose sand and soft clay-loose sand simulations at $\theta=60^{\circ}$. In the clay-sand simulations, an increase in the proportion of clay reduces the width of the surface distortion zone at U/H=30% or 40% past the critical U_{cr}/H at which the fault is fully ruptured. Once the fault is fully ruptured at U_{cr}/H , the width of the surface distortion zone is similar, although this is at substantially greater bedrock displacement for the simulations with greater clay proportion. Overall, since the clay delays the emergence of the main through-going shear band or fault across the soil deposit, much greater bedrock displacement is required to reach equivalent levels of surface distortion as the proportion of clay is increased in the simulations. Furthermore, since the formation of tension cracks with a greater proportion of clay actually concentrates deformation along the top surface of the hanging wall, the region of surface distortion is further reduced when compared to the conjugate extensional faulting which otherwise forms.

Similarly, on the foot wall side, additional clay fraction diminishes the number of faults rupturing at the surface, converging to a single fault in the CL10S0 simulation, further decreasing the size of W.

In the soft rock-loose sand simulations an increase in the soft rock content suppresses the formation of extensional conjugate faulting on the hanging wall side because of the higher cohesion of the soft rock compared to the loose soil, while on the foot wall side, the number of fault surface ruptures is reduced, and overall, the wide shear zone seen in the predominantly loose sand models is now further localized. All these factors contribute to the reduced surface distortion zone width seen with a larger proportion of soft rock. Hence, for both cases RC and CL, increasing the cohesive lower layer has the effect of reducing the distortion width at higher slip displacement, albeit this phenomenon is more pronounced for the soft clay layer.

5 Fault rupture through the foundations of earthen embankments

While practical experience has shown that most earthen embankments, embankment dams, or levees are able to accommodate deformation associated with a fault rupturing in their foundations, and such events are quite rare in the historical record [69], under certain conditions, the integrity of earth structures can be significantly jeopardized. For instance, the rupture of a reverse fault with the fault trace spanning parallel and aligned to the axis of an embankment dam is especially risky, given the potential for the impermeable core of the dam to be substantially damaged over an extensive portion of the axial length of the embankment [42]. In this paper we simulate the rupture of a reverse fault located in bedrock underneath the foundations of a homogeneous embankment, and determine the resulting strain localization patterns within the embankment as well as any resulting damage to the embankment.

Three different model setups are utilized in which the embankment is made of a granular fill material (GF) and is underlain by either clay (CL) or sand (S) layers with rigid bedrock consisting of boundary particles underneath the soil. In the first setup (CL0S10+GF), the granular fill embankment overlies a layer consisting of 100% sand, in the second setup (CL10S0+GF) the embankment overlies a purely clay layer, and in the third setup (CL5S5+GF), the soil deposit underneath the embankment consists of a top half of sand and a bottom half of clay. Like in our previous simulations, the clays are modeled using the Modified Cam Clay (MCC) model whereas the sands and granular fill material employ the Drucker-Prager yield criterion. The values of the respective material parameters are summarized in Table 3 Note the stress initialization procedure is the same as that described in Section 3.4 and the fault orientation in the bedrock is again $\theta = 60^{\circ}$. The embankment has an abutment length of 45 m, a crest width of 40 m, and a height of 24 m. The soil deposit underlying the embankment has a depth of 20 m. For each setup, three distinct simulations (for a total of 9 simulations) are performed where the location of the fault in the bedrock is moved from directly below the foot of the left abutment (Location 1) to directly below the central axis of the embankment (Location 2) to directly below the foot of the right abutment (Location 3).

Figure 17 displays contours of the accumulated plastic strain ε_{acc}^p and colored marker layers for the CL0S10+GF simulations at different values of normalized vertical bedrock displacement (U/H) to highlight the zones of localized strain which emerge as the bedrock fault propagates at each of the three different fault locations. Figures 18 and 19 display the same information but for the CL10S0+GF and CL5S5+GF simulations respectively.

Table 3. Constitutive parameters for the different soil types in the fault rupture through an embankment simulations. Note GF stands for granular fill, S stands for sand, and CL stands for clay.

Parameter	GF	\mathbf{S}	$\overline{\mathbf{CL}}$
Initial density, ρ [kg/m ³]	1700	1750	1900
Peak internal friction angle, ϕ_{max} [°]	34	37	_
Residual internal friction angle, ϕ_{res} [°]	32	34	_
Peak dilation angle, ψ_{max} [°]	11	10	_
Residual dilation angle, $\psi_{\rm res}$ [°]	0	0	_
Threshold octahedral plastic strain, γ_f^p	0.03	0.02	_
Cohesion, c [kPa]	30	0	_
Young's Modulus, E [MPa]	20	20	_
Poisson Ratio, ν	0.3	0.3	0.3
Initial OCR ratio,	f(y)	f(y)	f(y)
Critical state line slope, M	_	_	1.5
Initial void ratio, e	_	_	0.65
Virgin isotropic consolidation index, λ	_	_	0.3
Swelling index, κ	_	_	0.05

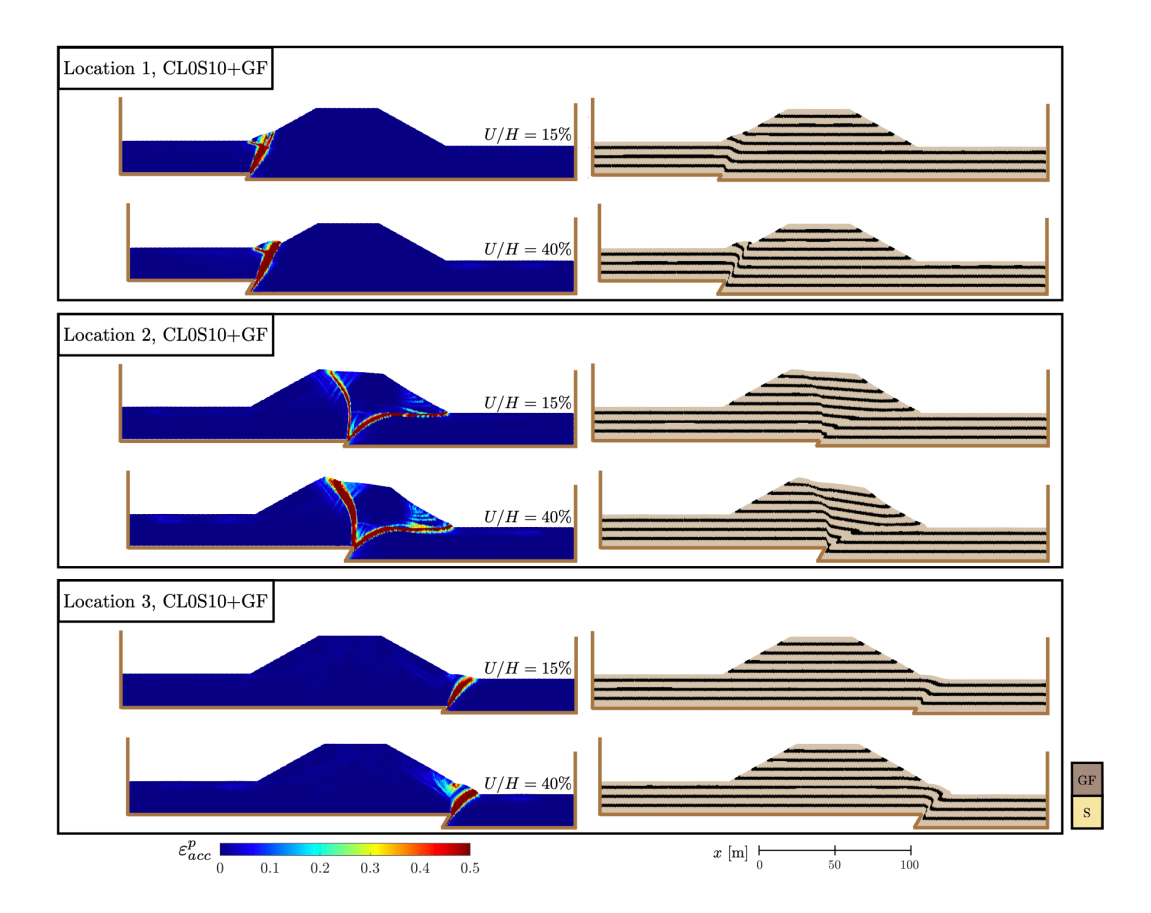


Fig. 17. Contours of the accumulated plastic strain ε_{acc}^p are shown on the left and deformed colored layers are shown on the right for the CL0S10+GF simulation at U/H=15 and U/H=40% at the three fault locations. Vertical bar on the bottom right indicates the soil deposit layering and embankment makeup.

At fault Location 1 for the CL0S10+GF model, the resulting fault propagates through a zone of mostly horizontal σ_1 as seen by the values of $\alpha=0^{\circ}$ in the first row of Figure [20]. The resulting fault takes an initial orientation close to 67° with respect to the horizontal as it propagates across the soil deposit underlying the embankment. Its rotation with respect to the horizontal is stymied by the presence of the embankment abutment, which reorients the direction of σ_1 parallel to the abutment slope, leading to an orientation with respect to σ_1 which is close to $\Theta=37\approx\Theta_{R,max}$ at U/H=15%, evolving to $\Theta=32\approx\Theta_{A,max}$ at U/H=40%. As the fault enters the foot of the embankment abutment, and since it does not rotate significantly with respect to the horizontal, a zone of uplift forms resulting in a small secondary conjugate localized plastic zone delimiting the uplifted bulge. Similar behavior is observed across all Location 1 simulations for both CL10S0+GF and CL5S5+GF cases as well.

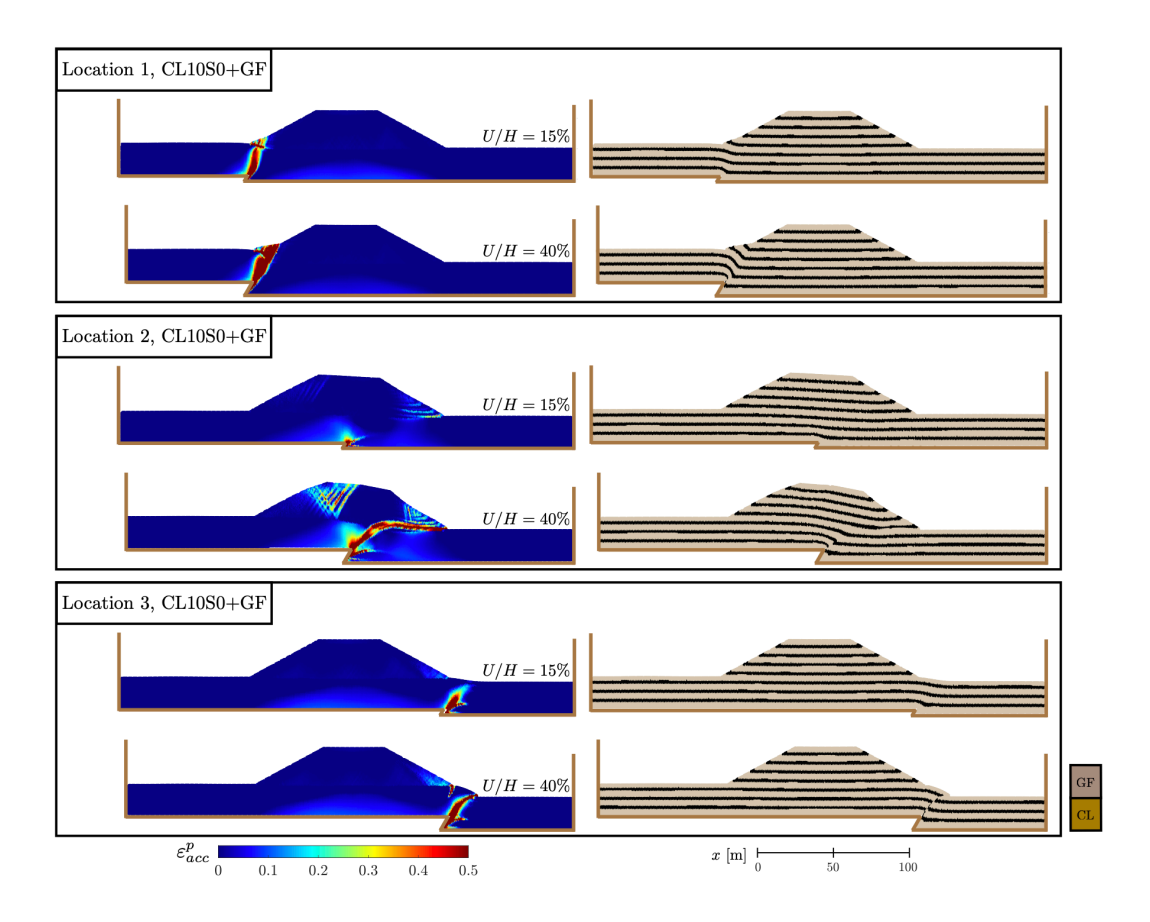


Fig. 18. Same as Figure 17 but for the CL10S0+GF simulation.

In the simulation with fault location 2 and the CL0S10+GF model, the primary fault rotates towards the horizontal as it propagates eventually rupturing at the toe of the right abutment of the embankment while a secondary fault propagates antithetically to the main one, rupturing the surface of the embankment at the crest. The behavior of the primary fault is mirrored in the CL10S0+GF and CL5S5+GF models, although that of the secondary antithetic fault is not, as it fails to propagate throughout the embankment in both simulations. Instead more diffuse zones of plastic strain form near the embankment axis. Additionally, in the CL10S0+GF case, we witness the formation of a stunted shear band (no discontinuity or offset across it) prior to the propagation of the eventually through-going primary

fault, as previously seen in clay dominated simulations. Another interesting feature of Location 2 faulting simulations, is a case of incipient abutment slope failure on the right abutment just above the fault scarp.

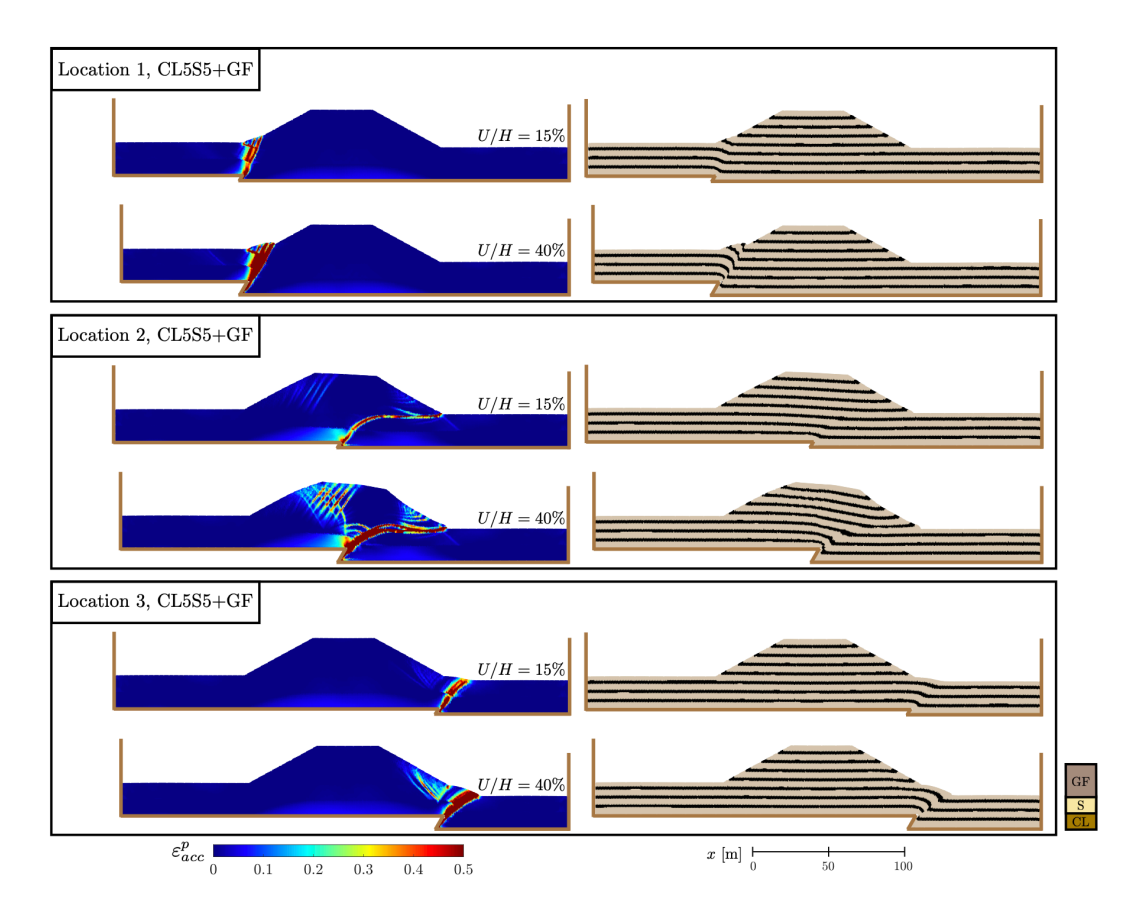


Fig. 19. Same as Figure 17 but for the CL5S5+GF simulation.

In the fault location 3 simulations, the emerging zone of strain localization is initially oriented at approximately $\Theta=65^{\circ}$ with respect to the horizontal and then decreases in steepness as it ruptures at the surface. In the CL10S0+GF simulation we observe the propagation of a stunted shear band on the foot wall side, which does not fully propagate across the soil deposit taking a final inclination of $\Theta=\Theta_{c,cs}$, and is superseded by the final through-going fault. As seen in the third row of Figure 20, the stunted shear band propagates through a zone of $\alpha=0^{\circ}$ on the footwall, whereas α increases near the surface rupture zone of the final through-going fault increasing slightly, but not sufficiently to fully explain the fault rotation without accounting for the influence of rigid body rotation of the fault. As seen in all three layered model setups but especially CL0S10+GF and CL5S5+GF, the fault scarp uplift near the embankment abutment toe weakens the abutment, causing a small slope failure. In CL10S0+GF, the tension crack which forms as a result of the significant folding of the clay layer underlying the embankment actually stabilizes the abutment, as it detaches the ongoing deformation caused by the fault from the rest of the embankment.

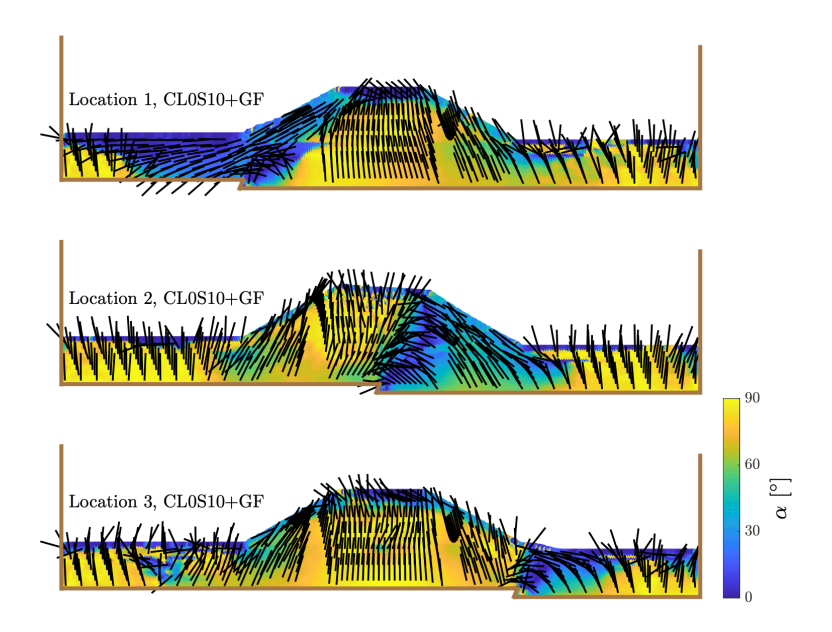


Fig. 20. Contours of deviation angle α of the direction of σ_1 from the horizontal with vectors indicating the σ_1 direction superimposed for simulation CL0S10+F at U/H = 15%.

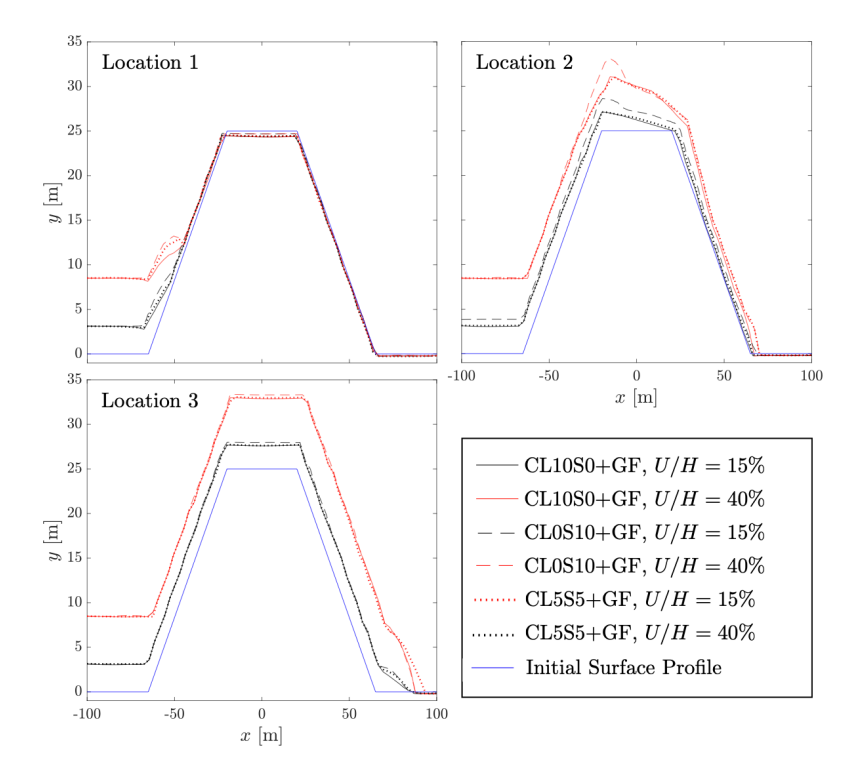


Fig. 21. Surface profiles for the three soil-embankment setups at two different values of normalized bedrock displacement.

In Figure [21], the surface profiles of the soil-embankment setups are plotted at different amounts of normalized vertical bedrock displacement relative to the initial surface profile for all simulations. As can be seen, fault location 3 produces the greatest amount of vertical uplift across the three model types, as moving the fault location farther to the right increases the portion of the embankment displaced as part of the hanging wall of the reverse fault. Location 1 shows the least amount of displacement, with some deformation and vertical uplift at the toe of the left abutment, and some slight depression of the embankment crest zone. Lastly, faulting location 2 causes a substantial amount of uplift, especially as a product of the scarp formed by the surface rupture of the secondary antithetic fault. In all faulting locations, the CL0S10+GF simulation with a 100% loose sand layer underlying the embankment obtains the largest vertical uplift, with CL10S0+GF the pure clay layer, generally the least, and CL5S5+GF in between these extremes. This behavior is consistent with our previous observation that soft clay helps to absorb the deformation imparted by bedrock fault slip seen in Section [4].

Another way to quantify the extent of embankment distortion or damage, in the wake of fault rupture, is the relative compaction of the embankment material. The relative compaction (RC) is the ratio between the in-situ dry density of the embankment granular fill material and the maximum dry density of the same material. The relative compaction between the initial RC_i and final RC_f states, can be expressed in terms of the change of volumetric strain of the soil $\Delta \varepsilon_v$ between the two states as such,

$$\Delta \varepsilon_v = \frac{RC_i}{RC_f} - 1. \tag{26}$$

The continued functionality of embankment fill can be determined in terms of the relative compaction threshold of RC >= 94%, with any portion possessing an RC less than 94% requiring repair [59]. To determine the relative compaction of the embankment, an initial RC = 95% is assumed in our simulations after stress initialization prior to fault loading which represents a typical value for a properly compacted generic granular fill road embankment. Then, given this initial value, the relative compaction at any point in time can be calculated using Eq. [26]. In Figure [22], the discrete probability density functions (PDFs) of RC are displayed for all particles encompassing the embankment with a vertical line denoting RC = 94%.

Defining the percentage of the embankment whose relative compaction is below the 94% threshold and requiring repair as RC_{94} (values summarized for each simulation in the caption of Figure [22]), it is evident that faulting location 2 is the most damaging, because a large portion of the embankment is subjected to fault displacement, and two main shear bands are generated compared to Location 1. Location 3, while encompassing much of the embankment, displaces it rigidly, therefore only the surface profile is uplifted, and less internal deformation occurs compared to Location 2. Interestingly, it is the CL5S5+GF model which records the greatest RC_{94} for locations 2 and 3, with $RC_{94} = 40.75\%$ and $RC_{94} = 8.07\%$ respectively. We see that, in general, the presence of clay in the underlying soil deposit, despite absorbing deformation as seen in the surface profiles, tends to increase the amount of relative compaction. However, as seen in CL10S0+GF, Location 3, the presence of the tension crack stabilizes the failing right abutment, which is not the case in the CL5S5+GF model, leading to greater deformation and a higher RC_{94} value in the latter. At faulting location 2, the RC_{94} is larger in the CL5S5+GF than in the CL10S0+GF simulation, because the antithetic shear band does not fully form in the latter case. The ability of clay to retard deformation is also seen in the generally higher RC_{94} of the sand dominated models at lower bedrock displacement (U/H = 15%), which ceases to be true at greater displacements, as seen at U/H = 40%, where the RC_{94} of the sand dominated models is surpassed by that of the simulations with clay layering.

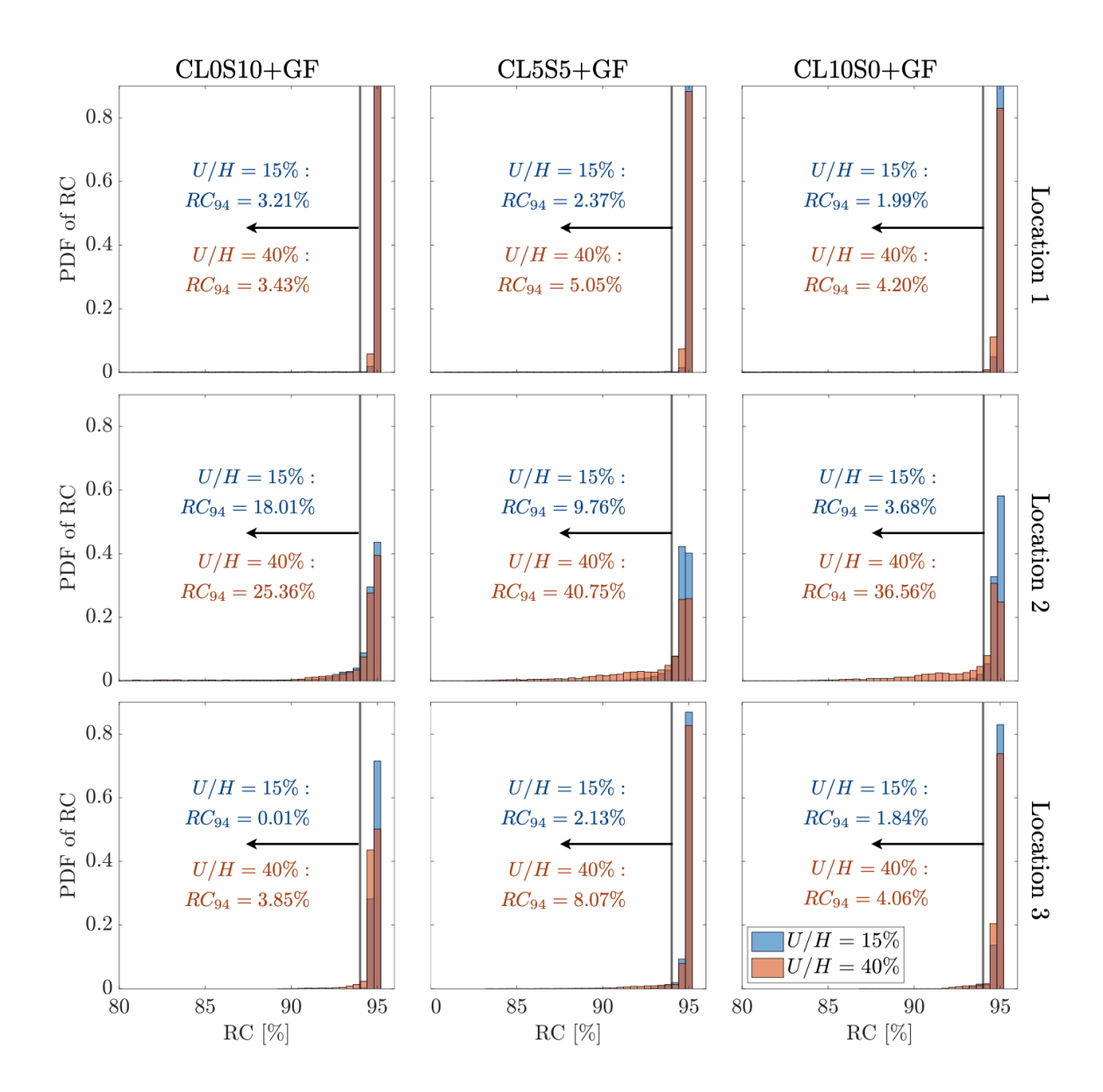


Fig. 22. Discrete probability density functions (PDFs) of relative compaction RC in each of the 9 simulations. First column is CL0S10+GF, second column is CL5S5+GF, and third column is CL10S0+GF, whereas the first row is faulting location 1, second row location 2, and third row location 3. PDFs are shown at both 15 and 40% normalized vertical bedrock displacement U/H.

6 Discussion

In the experimental setup of our simulations, we isolated the effects of rigid body rotation from strain softening on the fault or shear band orientations at large amounts of vertical bedrock fault displacement (or fault slip). In regions unaffected by the rigid body rotation induced by the progressive fault bedrock displacement, such as the foot wall, faults or shear bands generally stabilize at Coulomb orientations

given at the residual or critical state friction angle $(\Theta_{C,res}, \Theta_{C,cs})$. On the other hand, faults in the main through-going shear zone and in parts of the hanging wall side experience substantial rotation past the Coulomb orientation (i.e., shallower than Θ_C) with respect to the σ_1 direction after the faults have fully propagated through the soil deposit. The initial angle taken by the faults when forming from the base and propagating upwards is dependent on the angle of the fault in the bedrock (θ) , but the angle at which the fault is fully ruptured through the soil deposit is generally close to the Roscoe angle, making use of the peak friction and dilatancy angles $\Theta_{R,max}$, as long as the fault does not emerge as a bifurcation near the top surface from an existing previously rotated fault, and is thus independent of θ .

A considerable number of bifurcations occur at the interface boundary between respective soil types, for example, RC5S5s-F2cS and RC5S5s-F2aS in the soft rock-loose sand, or CL9S1-F3cS and CL9S1-F4aS in the soft clay-loose sand simulations. We also observe that the loose sand layers hold a predisposition towards bifurcations of the through-going faults when it overlies a layer of soft rock (e.g., RC7S3s-F2aS and RC7S3s-F2bS, or RC5S5s-F2aS and RC5S5s-F2bS), especially in proximity to the top ground surface. The vast majority of bifurcations however, propagate from the tip of the bedrock fault or slightly above it within the bottom soil layer whenever the existing main fault through the soil has rotated exceedingly shallowly (to a Coulomb orientation), such that it is no longer favorable to accommodate the vertical displacement of the bedrock fault.

We see that a number of factors can arrest the creation of such stunted faults, such as adding a larger proportion of soft rock to the layered soil (i.e., an increase in cohesion) concentrating the shear zone into a more limited region. The modified Cam Clay model, used to represent the soft clays in our simulations, seems best suited for capturing this phenomenon widely seen in analogue 1-g and centrifuge experiments. Not only do the stunted faults reach critical Coulomb orientations ($\Theta_{C,cs}$) once they cease growing, but the faults or shear bands reach the critical state line as evidenced in the p-q and $\log(p)-e$ history plots. Moreover, faults unload after they have fully propagated, proceeding with a softening and dilative response, all consistent with experimental observations. The MCC model also captures other important attributes of clay-like materials, for example, tensile cracking near the monocline hinge and the reticence of the clay to localization and through-going fault rupture, instead behaving with considerable ductility, absorbing the deformation of the bedrock fault.

The degree of overconsolidation of the soil also plays a decisive role in the performance of the clay soil in the MCC model. A higher OCR ratio will expand the size of the yield surface and the elastic zone, preventing accumulation of plastic strains, and the onset of localization. In the simulations in this paper, a realistic OCR depth profile has been assumed where the OCR ratio of the soil decreases towards OCR=1 with depth. In Figure 23 the results of simulations with varying OCR ratio are compared given the CL5S5 simulation set up. Specifically, the distribution of OCR ratio with depth OCR=f(y) assumed throughout the paper is compared with simulations where the OCR ratio is constant with depth. Increasing the OCR ratio at depth all the way to OCR=10, appreciably narrows the thickness of the shear zone emanating from the bedrock fault tip, and hinders the development of any stunted faults.

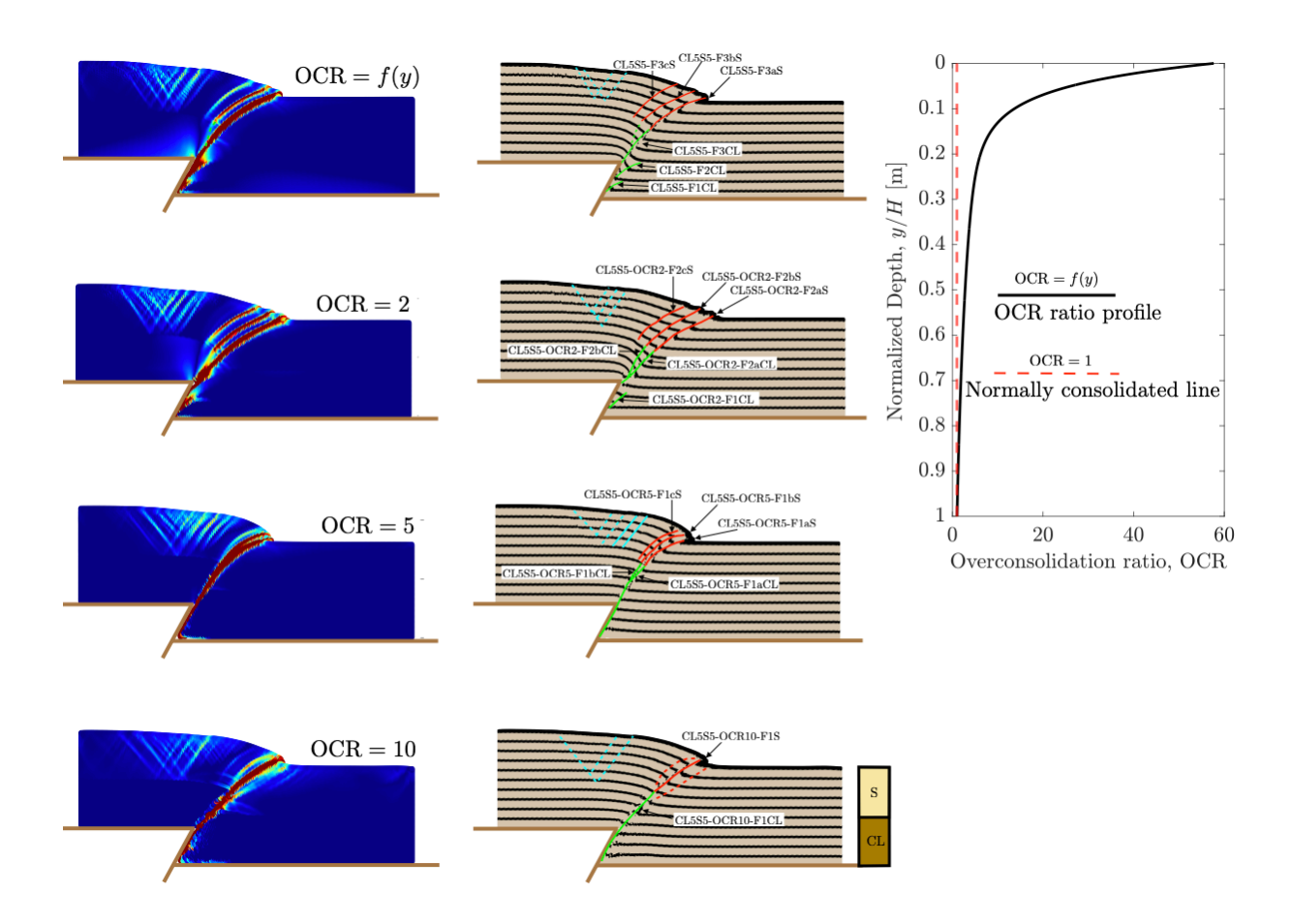


Fig. 23. Visualizations of the accumulated plastic strain ε_{acc}^p contours and deformed colored layers for the soft clay-sand simulations considering different overconsolidation ratios (OCR). In the topmost row, the OCR ratio is a function of depth OCR=f(y) and the dependence is shown on the right hand side plot. All simulations performed use the CL5S5 setup (bottom 50% clay, top 50% sand).

Lastly, a number of conclusions can be drawn for the practicing engineer. For example, the reduction in the fault surface distortion zone and the general absence of sharp fault scarps presented by clay as opposed to sand deposits may be advantageous when designing structures overlying or in the vicinity of active faults. Nevertheless, the presence of the extensive tensile stresses leading to tensile crack formation, and the widening of these cracks over progressive vertical bedrock fault displacement, presents a significant challenge, particularly towards shallowly-buried segmented water and sewer pipelines. In the 1994 Northridge Earthquake, tension cracks due to fault surface rupture were responsible for severing the joints of pipelines in various areas of the San Fernando Valley rendering them inoperable 36. The vertical bedrock fault displacement required for the fault to rupture and outcrop at the surface is also an important parameter for determining the potential hazard of buried faults in bedrock. If the ultimate fault slip ends up being less than the critical amount required for surface outcropping when the fault eventually ruptures, any structures near the surface will only experience a relatively smooth surface uplift distribution, which would be substantially less damaging than the scarp which would otherwise develop. In addition, the structures would be exposed to a significantly lesser amount of surface uplift in this scenario. In our simulations, we see that clay-dominated layered soil deposits experience greater normalized critical bedrock displacement U_{cr}/H , reducing the risk for any overlying structures and utilities when

compared to soil deposits dominated by loose sand. The increase in proportion of soft clay relative to loose sand also reduces the extent of the surface distortion zone post-surface rupture, permitting less restrictive construction closer to the predicted fault scarp location.

Such results and understanding gained from fault rupture across multilayered soil deposits can be used to inform and comprehend what is happening in the more complicated simulations investigating fault rupture in the foundations of an earthen embankment. While the re-aligning of principal stress directions with the embankment abutments substantially affects the propagation paths and inclination of the resulting localized strain zones, surface rupture continues to generally occur at $\Theta_{R,max}$ with respect to the σ_1 direction, and in clay strata, stunted bands achieve orientations consistent with $\Theta_{C,cs}$. Furthermore, the ability of clay to absorb deformation caused by fault displacement, and the formation of tensile cracks along fold hinge lines is also manifested in the embankment simulations. The significant differences in damage sustained by the embankments, surface profile uplift, and in the number and trajectory of resulting shear bands, as a result of fault location and varying soil stratification, reinforces the need to design embankments and other earthen structures not only against the dynamic oscillation of earthquakes, but also against fault slip induced displacement.

7 Conclusion

This paper tackles fault rupture through layered clay-sand deposits, which are a more realistic representation of most in-situ soils subjected to shallow fault rupture compared to homogeneous sand deposits predominantly considered in the literature. The paper also explores the possibility of fault rupture beneath an earthen embankment. By using the Modified Cam Clay model appropriate for soft clays, in combination with a meshfree continuum particle method, Smoothed Particle Hydrodynamics, the critical state behavior of overconsolidated soil undergoing large deformations was simulated, providing new insights into the fault rupture process and its consequences in these types of soil conditions. In homogenous and stratified soil, we conclude that faults or shear bands obtain and maintain Coulomb orientations given the residual or critical state friction angle whereas rotations past such values typically occur on faults or shear bands on the hanging wall side of the fault and are caused by rigid body rotation of the soil. We also observe that varying the relative thickness of sand and clay layers in stratified soils affects the width of the surface distortion zone as well as the critical amount of bedrock displacement for surface rupture to occur. In addition, the frequency of stunted faults, tension cracks, and bifurcated faults or shear bands is also sensitive to soil stratification and the relative thickness of the sand and clay layers. Lastly, the paper shows that the SPH method, through its numerical non-locality, helps eliminate the dependency of localization and the softening response on the discretization resolution, a fact which underlines the chosen computational approach's significant advantages for any future studies involving strain localization and faulting in geomaterials.

Acknowledgements

This material is based upon work supported by the National Science Foundation under Award Number CMMI-1914780. The first author acknowledges the support by the U.S. National Science Foundation (NSF) Graduate Research Fellowship under Grant DGE 1656518, as well as by the Stanford Graduate Fellowship.

References

[1] Abrari Vajari, S., Neuner, M., Arunachala, P. K., Ziccarelli, A., Deierlein, G., Linder, C.: A thermodynamically consistent finite strain phase field approach to ductile fracture considering multi-axial stress states. *Computer Methods in Applied Mechanics and Engineering* **400**, 115467 (2022)

- [2] Adami S, Hu XY, Adams NA. A generalized wall boundary condition for smoothed particle hydrodynamics. *Journal of Computational Physics* 2012, 231, pp. 7057-7075.
- [3] Ahmadi, M., Moosavi, M., Jafari, M.K.: Experimental investigation of reverse fault rupture propagation through cohessive granular soils. *Geomechanics for Energy and Environment* 14, 61–65 (2018)
- [4] Ahmadi, M., Moosavi, M., Jafari, M.K.: Experimental investigation of reverse fault rupture propagation through wet granular soil. *Engineering Geology* **239**, 229–240 (2018)
- [5] Anastasopoulos, I., Callerio, A., Bransby, M.F., Davies, M.C.R., Nahas, A.E., Faccioli, E., Gazetas, G., Masella, A., Paloucci, R., Pecker, A., Rossignol, E.: Numerical analyses of fault-foundation interaction. *Bulletin of Earthquake Engineering* 6, 645–675 (2008)
- [6] Anastasopoulos, I., Gazetas, G., Bransby, M.F., Davies, M.C.R., Nahas, A.E.: Fault rupture propagation through sand: Finite-element analysis and validation through centrifuge experiments. *Journal of Geotechnical and Geoenvironmental Engineering* 133(8), 943–958 (2007)
- [7] Anastasopoulos, I., Gerolymos, N., Drosos, V., Georgarakos, T., Kourkoulis, R., Gazetas, G.: Behavior of deep immersed tunnel under combined normal fault rupture deformation and subsequent seismic shaking. *Bulletin of Earthquake Engineering* **6**, 213–239 (2008)
- [8] Borja, R.I., Lee, S.R.: Cam-Clay plasticity, Part I: Implicit integration of elasto-plastic constitutive relations. Computer Methods in Applied Mechanics and Engineering 78(1), 49–72 (1990)
- [9] Borja, R.I., Regueiro, R.A.: Strain localization in frictional materials exhibiting displacement jumps. Computer Methods in Applied Mechanics and Engineering 190(20–21), 2555–2580 (2001)
- [10] Borja RI. Plasticity Modeling & Computation. Springer, Berlin-Heidelberg.
- [11] Borja, R. I., Chen, W., Odufisan, A. R.: A constitutive framework for rocks undergoing solid dissolution. *Journal of the Mechanics and Physics of Solids* **173**, 105198 (2023)
- [12] Bray, J.D., Seed, R.B., Cluff, L.S., Seed, H.B.: Earthquake fault rupture propagation through soil. Journal of Geotechnical Engineering 120(3), 543–561 (1994)
- [13] Bui, H.H., Fukagawa, R., Sako, K., Ohno, S.: Lagrangian meshfree particles method (SPH) for large deformation and failure flows of geomaterial using elastic-plastic soil constitutive model. *International Journal for Numerical and Analytical Methods in Geomechanics* 32, 1537–1570 (2008)
- [14] Bui, H.H., Nguyen, G.D.: Smoothed particle hydrodynamics (SPH) and its applications in geomechanics: From solid fracture to granular behavior and multiphase flows in porous media. Computers and Geotechnics 138, 104315 (2021)
- [15] Cai, Q.P., Peng, J.M., Ng, C.W.W., Shi, J.W., Chen, X.X.: Centrifuge and numerical modelling of tunnel intersected by normal fault rupture in sand. Computers and Geotechnics 111, 137–146 (2019)
- [16] Chen, Y., Mobasher, M. E., Gu, C., Zheng, D., Waisman, H.: Thermodynamically consistent non-local damage formulation for fluid-driven fracture in poro-viscoelastic media. Acta Geotechnica 17, 5321–5350 (2022)
- [17] Chen, X., Shi, C., Jia, Y., Zhang, Y-P., Ruan, H-N.: Numerical study on seepage properties of rock mass withnon-penetrating fracture using discrete element method. *International Journal for Numerical and Analytical Methods in Geomechanics* 48, 287–310 (2023)
- [18] Cole, D.A., Lade, P.V.: Influence zones in alluvium over dip-slip faults. Journal of Geotechnical Engineering 110(5), 599–615 (1984)
- [19] Copana, J.S., Garcia, F.E.: Continuum-based modeling of earthquake fault rupture propagation through layered soils. In: T.M. Evans, N. Stark, S. Chang (eds.) Geo-Congress 2024, Geo-Institute of ASCE, 440–449 (2024)
- [20] Coulomb, C.A.: Essai sur une application des regles des maximis et minimis a quelques problemes de statique relatifs a l'architecture. *Memoires de l'Academie Royale pres Divers Savants* 7, (1776)
- [21] Chen X, Leung Y, Mori H, Uchida S, Takumi K. Single-layer soil-water coupled SPH method and its application to sinkhole simulation. *Acta Geotechnica* (2023)
- [22] del Castillo, E.M., Fávero Neto, A.H., Borja, R.I.: A continuum meshfree method for sandbox-style numerical modeling: Application to accretionary and doubly vergent wedges. *Journal of Structural Geology* **153**, 104466 (2021)

- [23] del Castillo, E.M., Fávero Neto, A.H., Borja, R.I.: Fault propagation and surface rupture in geologic materials with a meshfree continuum method. *Acta Geotechnica* **16**, 2463–2486 (2021)
- [24] del Castillo E.M., Fávero Neto A.H., Borja R.I.: Modeling Fault Rupture Through Layered Geomaterials with SPH. In: Dyskin A, Pasternak E., eds. Multiscale Processes of Instability, Deformation and Fracturing in Geomaterials, Springer Series in Geomechanics and Geoengineering. IWBDG 2022. Springer, Cham; (2023)
- [25] del Castillo, E.M., Fávero Neto, A.H., Geng, J., Borja, R.I.: An SPH framework for drained and undrained loading over large deformations. *International Journal for Analytical and Numerical* Methods in Geomechanics 48(12), 3227-3257 (2024)
- [26] del Castillo, E.M., Ferdowsi, B., Rubin, A.M., Schoene, B.: Strain localization patterns and thrust propagation in 3-D discrete element method (dem) models of accretionary wedges. *Tectonics* 42(8), e2022TC007707 (2023)
- [27] del Castillo, E.M., Geng, J., Borja, R.I.: A nonlocal kernel-based continuum damage model for compaction band formation in porous sedimentary rock. *Computational Mechanics* (2024) https://doi.org/10.1007/s00466-024-02540-x
- [28] Fávero Neto, A.H.: A continuum Lagrangian finite deformation computational framework for modeling granular flows. Ph.D. thesis, Stanford University (2020)
- [29] Fei, F., Mia Shumon M., Elbanna, A.E., Choo, J.: Phase-field model for quasi-dynamic nucleation, growth, and propagation of rate-and-state faults. *International Journal for Numerical and Analyt*ical Methods in Geomechanics 47(2), 187–211 (2022)
- [30] Garcia, F.E., Bray, J.D.: Distinct element simulations of shear rupture in dilatant granular media. *International Journal of Geomechanics* **18**(9), 04018111 (2018)
- [31] Garcia, F.E., Bray, J.D.: Discrete element analysis of earthquake surface fault rupture through layered media. *Soil Dynamics and Earthquake Engineering* **152**, 107021 (2022)
- [32] Gao L, Pastor M, Li T, et al. A framework coupled neural networks and SPH depth integrated model for landslide propagation warning. Acta Geotechnica 18, 3863–3888 (2023)
- [33] Gingold, R., Monaghan, J.: Smoothed particle hydrodynamics: theory and application to nonspherical stars. *Monthly Notices of the Royal Astronomical Society* **181**, 375–389 (1977)
- [34] Gray, J., Monaghan, J.J.: SPH elastic dynamics. Computer Methods in Applied Mechanics and Engineering 190(49–50), 6641-6662 (2001).
- [35] Hazeghian, M., Soroush, A.: DEM-aided study of Coulomb and Roscoe theories for shear band inclination. *Acta Geotechnica* 17, 3357–3375 (2022)
- [36] Holzer, T.L., Bennett, M.J., Ponti, D.J., III, J.C.T.: Liquefaction and soil failure during 1994 Northridge earthquake. Journal of Geotechnical and Geoenvironmental Engineering 125(6), 438–452 (1999)
- [37] Hong, Y., Zhang, J., Zhao, Y., Wang, L., Wang, L.: Coupled hydro-mechanical XFEM analysis for multi-fracturing through an excavation driven by an underlying aquifer: a forensic case study. Acta Geotechnica (2023)
- [38] Hung, W.Y., Soegianto, D.P., Wang, Y.H., Huang, J.X.: Reverse fault slip through soft rock and sand strata by centrifuge modeling tests. Acta Geotechnica 17, 3337–3356 (2022)
- [39] Ip, S.C.Y., Borja, R.I.: A phase-field approach for compaction band formation due to grain crushing. International Journal for Numerical and Analytical Methods in Geomechanics 46(16), 2965–2987 (2022)
- [40] Ip, S.C.Y., Borja, R.I.: Modeling heterogeneity and permeability evolution in a compaction band using a phase-field approach. *Journal of the Mechanics and Physics of Solids* **181**, 105441 (2023)
- [41] Karabacak, V., Ozkaymak, Ç., Sözbilir, H., Tatar, O., Aktuğ, B., Ozdağ, O.C., Çakir, R., Aksoy, E., Koçbulut, F., Softa, M., Akgün, E., Demir, A., Arslan, G.: The 2023 Pazarcık (Kahramanmaraş, Türkiye) earthquake (Mw 7.7): implications for surface rupture dynamics along the East Anatolian Fault Zone. Journal of the Geological Society 180(3), jgs2023-020 (2023).
- [42] Lazarte, C.A.: The response of earth structures to surface fault rupture. Ph.D. thesis, University of California at Berkeley (1996)

- [43] Lee, J.W., Hamada, M.: An experimental study on earthquake fault rupture propagation through a sandy soil deposit. *Structural Engineering/Earthquake Enginnering JSCE* **22**(1), 1s–13s (2005)
- [44] Liao, P., Guo, C., Wang, F., Sun, W., Ni., P.: Investigating brittle damage of buried pipelines under dip-slip faulting with peridynamics. Acta Geotechnica 18, 1945–1965 (2023)
- [45] Li Y., Liu H.Q., Yang L., Liu Y.: An optimized DEM-SPH model for surge waves induced by riverside landslides. *International Journal for Numerical and Analytical Methods in Geomechanics* 48(1), 270–286 (2023)
- [46] Lin, M.L., Chung, C.F., Jeng, F.S.: Deformation of overburden soil induced by thrust fault slip. Engineering Geology 88(1-2), 70–89 (2006)
- [47] Liu F., Borja R.I.: Stabilized low-order finite elements for frictional contact with the extended finite element method. Computer Methods in Applied Mechanics and Engineering 199(37-40), 2456–2471 (2010)
- [48] Liu, C.Y., Li, C.H., Chan, P.C., Hung, C.H., Lin, M.L.: 3D sandbox and numerical modeling of coseismic surface rupture induced by oblique-slip fautling and its interaction with embedded shallow foundation. *Engineering Geology* 282, 105990 (2021)
- [49] Liu G, Liu M. Smoothed Particle Hydrodynamics: A Meshfree Particle Method. World Scientific Co., 2003.
- [50] Loukidis, D., Bouckovalas, G.D., Papadimitriou, A.G.: Analysis of fault rupture propagation through uniform soil cover. Soil Dynamics and Earthquake Engineering 29(11-12), 1389–1404 (2009)
- [51] Lucy, L.B.: A numerical approach to the testing of the fission hypothesis. *The Astronomical Journal* 82(12), 1013–1024 (1977)
- [52] Mu D, Tang A, Li Z, Qu H, Huang D. A bond-based smoothed particle hydrodynamics considering frictional contact effect for simulating rock fracture. Acta Geotechnica 18, 625–649 (2023)
- [53] Muhlhaus, H., Vardoulakis, I.: The thickness of shear bands in granular materials. *Géotechnique* 37(3), 271–283 (1987)
- [54] Mullet, B., Segall, P., Neto, A.F.: Numerical modeling of caldera formation using Smoothed Particle Hydrodynamics (SPH). Geophysical Journal International 234(2), 887–902 (2023)
- [55] Mukhtar, F. M., Shauer, N., Duarte, C.A.: Propagation mechanisms and parametric influence in multiple interacting hydraulic fractures: A 3-D G/XFEM hydro-mechanical modeling. *International Journal for Numerical and Analytical Methods in Geomechanics* 46(11), 2033–2059 (2022)
- [56] Neuner, M., Abrari Vajari, S., Arunachala, P. K., Linder, C.: A better understanding of the mechanics of borehole breakout utilizing a finite strain gradient-enhanced micropolar continuum model. Computers and Geotechnics 153, 105064 (2022)
- [57] Oettle, N.K., Bray, J.D., Dreger, D.S.: Dynamic effects of surface fault rupture interaction with structures. *Soil Dynamics and Earthquake Engineering* **72**, 37–47 (2015)
- [58] Pastor M, Tayyebi S.M., Stickle M.M., et al.: An Arbitrary Lagrangian Eulerian (ALE) finite difference (FD)-SPH depth integrated model for pore pressure evolution on landslides over erodible terrains. *International Journal for Numerical and Analytical Methods in Geomechanics* 46(6), 1127– 1153 (2022)
- [59] Petela, E., Klimis, N.S.: Numerical assessment of distortion and damage induced on a highway embankment due to reverse fault rupture propagation. Soil Dynamics and Earthquake Engineering 116, 264–277 (2019)
- [60] Plafker, G.: Surface faults on Montague Island associated with the 1964 Alaska earthquake. U.S. Geological Survey Professional Paper 543-G, G1–G42 (1967)
- [61] Ramachandran, P., Puri, K., Bhosale, A., Dinesh, A., Muta, A., Negi, P., Govind, R., Sanka, S., Pandey, P., Kaushik, C., Kumar, A., Sen, A., Kaushik, R., Patil, M., Tavker, D., Menon, D., Kurapati, V., Sebastian, A.S., Dutt, A., Agarwal, A.: PySPH: a Python-based framework for smoothed particle hydrodynamics. ACM (2019)
- [62] Rattez, H., Shi, Y., Sac-Morane, A., Klaeyle, T., Mielniczuk, B., Veveakis, M.: Effect of grain size distribution on the shear band thickness evolution in sand. *Géotechnique* **72**(4), 350–363 (2022)

- [63] Reddy N. S. C., He, H., Senetakis, K.: DEM multi-scale insights on the pre-failure behavior of mature structured sands: Influence of bond type, amount, breakage pattern and heterogeneity. *International Journal for Numerical and Analytical Methods in Geomechanics* 47, 2587–2617 (2022)
- [64] Regueiro, R.A., Borja, R.I.: Plane strain finite element analysis of pressure sensitive plasticity with strong discontinuity. *International Journal of Solids and Structures* **38**(21), 3647–3672 (2001)
- [65] Roscoe, K.H.: The influence of strains in soil mechanics. Géotechnique 20(2), 129–170 (1970)
- [66] Roscoe K.H., Burland J.H.: On the generalized stress-strain behavior of 'wet' clay. In: Heyman J, Leckie FA., eds. Engineering PlasticityCambridge University Press; 535–609 (1968)
- [67] Sanz P.F., Borja R.I., Pollard D.D.: Mechanical aspects of thrust faulting driven by far-field compression and their implications for fold geometry. *Acta Geotechnica* 2, 17–31 (2007)
- [68] Sanz PF, Pollard D., Allwardt, P.F., Borja, R.I.: Mechanical models of fracture reactivation and slip on bedding surfaces during folding of the asymmetric anticline at Sheep Mountain, Wyoming. *Journal of Structural Geology* 30(9), 1177–1191 (2008)
- [69] Sherard, J.L., Cluff, L.S., Allen, C.R.: Potentially active faults in dam foundations. Géotechnique 3, 367–428 (1974)
- [70] Shi, J., Guan, L., Zhuang, D., Chen, X., Ling, D.: Fault rupture propagation in soil with intercalation using nonlocal model and softening modulus modification. *Journal of Rock Mechanics and Geotechnical Engineering* (2023)
- [71] Shi, J.S., Ling, D.S., Hu, C.B., bin Tu, F.: Study on reverse fault rupture propagation through sand with inclined ground surface. *Engineering Geology* **276**, 105768 (2020)
- [72] Shibuya, S., Mitachi, T., Tamate, S.: Interpretation of direct shear box testing of sands as quasisimple shear. *Géotechnique* **47**(4), 769–790 (1997)
- [73] Shirahama, Y., Yoshimi, M., Awata, Y., Maruyama, T., Azuma, T., Miyashita, Y., Mori, H., Imanishi, K., Takeda, N., Ochi, T., Otsubo, M., Asahina, D., Miyakawa, A.: Characteristics of the surface ruptures associated with the 2016 Kumamoto earthquake sequence, central Kyushu, Japan. Earth, Planets and Space 68(191) (2016)
- [74] Simo, J.C., Oliver, J., Armero, F.: An analysis of strong discontinuities induced by strain-softening in rate-independent inelastic solids *Computational Mechanics* 12, 227–296 (1993).
- [75] Suk Suh, H., Sun, W.: Multi-phase-field microporomechanics model for simulating ice-lens growth in frozen soil *International Journal for Numerical and Analytical Methods in Geomechanics* 46(12), 2307–2336 (2022)
- [76] Stone, K.J.L., Wood, D.M.: Effects of dilatancy and particle size observed in model tests on sand. Soils and Foundations 32(4), 43–57 (1992)
- [77] Tali, N., Lashkaripour, G.R., Moghadas, N.H., Ghalandarzadeh, A.: Centrifuge modeling of reverse fault rupture propagation through single-layered and stratified soil. *Engineering Geology* 249, 273– 389 (2019)
- [78] Violeau D. Fluid Mechanics and the SPH Method, Oxford University Press, 2012.
- [79] Wang, Y., Bui, H.H., Nguyen, G.D., Ranjith, P.G.: A new SPH-based continuum framework with an embedded fracture process zone for modelling rock fracture. *International Journal of Solids and Structures* **159**, 40–57 (2019)
- [80] Wang, Y., Javadi, A.A., Fidelibus, C.: A hydro-mechanically-coupled XFEM model for the injection-induced evolution of multiple fractures. *International Journal for Numerical and Analytical Methods in Geomechanics* 47(9), 1539–1558 (2023)
- [81] Wood, D.M.: Geotechnical Modelling. CRC Press (2004)
- [82] Wu, D., Ren, Z., Liu, J., Chen, J., Gup, P., Yin, G., Ran, H., Li, C., Yang, X.: Coseismic surface rupture during the 2018 Mw 7.5 Palu earthquake, Sulawesi Island, Indonesia. GSA Bulletin 133(5/6), 1157–1166 (2021)
- [83] Xiong H., Hao M., Zhao D., Qiu Y., Chen X. Study of the dynamics of water-enriched debris flow and its impact on slit-type barriers by a modified SPH–DEM coupling approach. *Acta Geotechnica* (2023) https://doi.org/10.1007/s11440-023-02106-w
- [84] Xiong, H., Qiu, Y., Shi, X., Wang, X., Chen, X.: Arching development above active trapdoor: insight from multi-scale analysis using FEM-SPH. *Acta Geotechnica* (2024)

- 40 Enrique M. del Castillo¹, Alomir H. Fávero Neto², and Ronaldo I. Borja^{1*}.
- [85] Yang, E., Bui, H., Sterck, H.D., Nguyen, G.: A scalable parallel computing SPH framework for predictions of geophysical granular flows. *Computers and Geotechnics* **121**, 103474 (2020)
- [86] Yang, H.W., Beeson, J.: The setback distance concept and the 1999 Chi-Chi (Taiwan) earthquake. In: International Conferences on Recent Advances in Geotechnical Earthquake Engineering and Soil Dynamics 29, (2001)
- [87] Yao, C., Takemura, J., Guo, W., Yan, Q.: Hyperbolic spiral model for predicting reverse fault ruptures in sand based on centrifuge tests. *Géotechnique* **71**(7), 571–582 (2021)
- [88] Yao, C., Zhang, Y., He, C., Yang, W., Yan, Q., Guo, D.: New insights into normal fault rupture propagation in sand. *Acta Geotechnica* (2023)
- [89] Zhang, Z., Feng, J., Zhu, Z., Zhao, Q., Pan, Y.; Analytical solution for buried pipeline deformation induced by normal and reverse fault considering structural joint influence *International Journal for Numerical and Analytical Methods in Geomechanics* (2024)